Available online at www.sciencedirect.com

ScienceDirect

Geochimica et Cosmochimica Acta 204 (2017) 83–103

Geochimica et Cosmochimica Acta

www.elsevier.com/locate/gca

Effect of pressure on $Fe^{3+}/\Sigma Fe$ ratio in a mafic magma and consequences for magma ocean redox gradients

H.L. Zhang [a,*], M.M. Hirschmann [a], E. Cottrell [b], A.C. Withers [a,c]

[a] Department of Earth Sciences, University of Minnesota, Minneapolis, MN 55455, USA
[b] Smithsonian Institution, National Museum of Natural History, Washington, DC 20560, USA
[c] Department of Earth Sciences, University of Western Ontario, London, Ontario N6A 5B7, Canada

Received 2 April 2016; accepted in revised form 11 January 2017; available online 23 January 2017

Abstract

Experiments establishing the effect of pressure on the $Fe^{3+}/\Sigma Fe$ ratio of andesitic silicate melts buffered by coexisting Ru and RuO_2 were performed from 100 kPa to 7 GPa and 1400–1750 °C. $Fe^{3+}/\Sigma Fe$ ratios were determined by room temperature Mössbauer spectroscopy, but corrected for the effects of recoilless fraction. $Fe^{3+}/\Sigma Fe$ ratios in quenched glasses decrease with increasing pressure consistent with previous results between 100 kPa and 3 GPa (O'Neill et al., 2006), but show only small pressure effects above 5 GPa. Ratios also decrease with increasing temperature. Mössbauer hyperfine parameters indicate mean coordination of Fe^{3+} ions of ~5 in glasses, with no dependence on the pressure from which the glasses were quenched, but show an increase with pressure in mean coordination of Fe^{2+} ions, from ~5 to ~6. XANES spectra on these glasses show variations in pre-edge intensities and centroid positions that are systematic with $Fe^{3+}/\Sigma Fe$, but are displaced from those established from otherwise identical andesitic glasses quenched at 100 kPa (Zhang et al., 2016). These systematics permit construction of a new XANES calibration curve relating pre-edge sub-peak intensities to $Fe^{3+}/\Sigma Fe$ applicable to high pressure glasses. Consistent with interpretations of the Mössbauer hyperfine parameters, XANES pre-edge peak features in high pressure glasses are owing chiefly to the effects of pressure on the coordination of Fe^{2+} ions from ~5.5 to ~6, with negligible effects evident for Fe^{3+} ions. We use the new data to construct a thermodynamic model relating the effects of oxygen fugacity and pressure on $Fe^{3+}/\Sigma Fe$. We apply this model to calculate variations in oxygen fugacity in isochemical (constant $Fe^{3+}/\Sigma Fe$) columns of magma representative of magma oceans, in which fO_2 is fixed at the base by equilibration with molten Fe. These calculations indicate that oxygen fugacities at the surface of shallow magma oceans are more reduced than at depth. For magma oceans in which the pressure at the base is near 5 GPa, as may be appropriate for Mercury and the Moon, conditions at the surface are ~1.5 log unit more reduced at the surface than at their base. If the results calibrated up to pressures of 7 GPa can be extrapolated to higher pressures appropriate for magma oceans on larger terrestrial planets such as Mars or Earth, then conditions at the surface are ~2 or 2.5 log units more reduced at the surface than at the base, respectively. Thus, atmospheres overlying shallow magma oceans should be highly reduced and rich in H_2 and CO.

Keywords: Magma Oceans; Oxidation state; Iron; Oxygen fugacity; Early atmosphere

1. INTRODUCTION

Owing to its importance to the chemical and physical properties of magmas, the relative concentration of Fe^{2+} and Fe^{3+} in natural and synthetic silicate liquids has received broad attention for at least 30 years (Sack et al.,

* Corresponding author.
E-mail address: hongluo@ustc.edu.cn (H.L. Zhang).

http://dx.doi.org/10.1016/j.gca.2017.01.023
0016-7037/

1980; Mysen and Virgo, 1985; Christie et al., 1986; Dingwell et al., 1988; Lange and Carmichael, 1989; Kress and Carmichael, 1991; Jayasuriya et al., 2004; Bézos et al., 2005; O'Neill et al., 2006; Borisov and McCammon, 2010; Cottrell and Kelley, 2011). In natural silicate melts, Fe is commonly the most abundant element with multiple oxidation states, and so the ratio of Fe^{3+} to total Fe, $Fe^{3+}/\Sigma Fe$, not only reflects but in many cases can establish the oxygen fugacity, fO_2, at magmatic conditions. The $Fe^{3+}/\Sigma Fe$ ratio increases with fO_2, but also is influenced by melt composition, temperature, and pressure (Kress and Carmichael, 1991; O'Neill et al., 2006; Borisov and McCammon, 2010). Of these variables, the effect of pressure has been least explored, and consequently Fe^{2+}-Fe^{3+} redox relationships in magmas at high pressures are poorly constrained.

A pressure dependence to the $Fe^{3+}/\Sigma Fe$ ratio in silicate liquids arises owing to differences in partial molar volumes of molten Fe_2O_3 and FeO (Rivers and Carmichael, 1987; Kress and Carmichael, 1991; Liu and Lange, 2006; O'Neill et al., 2006). As a consequence, compression or decompression of magmas with fixed $Fe^{3+}/\Sigma Fe$ can create variations in fO_2. For example, Kress and Carmichael (1991) and O'Neill et al. (2006) noted that basalts ascending from a shallow mantle source decrease in fO_2 compared to solid oxide buffers such as quartz-fayalite-magnetite (QFM). Magma oceans represent another environment in which changes in pressure can produce shifts in fO_2 relative to standard buffers (e.g., Hirschmann, 2012; Righter and Ghiorso, 2012a). Over the protracted history of planetary accretion and differentiation we may expect the oxygen fugacity of impactors and/or magma oceans to evolve (e.g. O'Neill, 1991; Rubie et al., 2015). Accretion events are brief, however, and at any particular time, a given convecting magma ocean can be isochemical if it is well-mixed and except at its base, metal free (Hirschmann, 2012). Hirschmann (2012) emphasized that redox gradients in magma oceans with fixed $Fe^{3+}/\Sigma Fe$ ratio may control the redox state and mass of early planetary atmospheres. Understanding oxygen fugacity gradients in magma oceans is the chief motivation for the present experimental study of the influence of pressure on $Fe^{3+}/\Sigma Fe$ ratio in magmas.

Oxygen fugacity is an important parameter influencing the composition and mass of atmospheres overlying planetary magma oceans because it controls the relative proportions of oxidized (H_2O, CO_2, N_2) and reduced (H_2, CO, NH_3) species in a high temperature magmatic vapor, and because differential solubility of these species (Pawley et al., 1992; Hirschmann, 2012; Wetzel et al., 2013; Chi et al., 2014; Stanley et al., 2014; Armstrong et al., 2015) affects the proportion of volatiles sequestered in the magma ocean (Hirschmann, 2012). Further, oxygen fugacity prevailing during silicate-metal separation in magma oceans determines the fraction of atmophile elements (H,C,N) sequestered in the core (Stevenson, 1977; Ohtani et al., 2005; Dasgupta et al., 2013; Roskosz et al., 2013) and thereby removed from possible liberation to the atmosphere.

Where silicate in magma oceans reacts with Fe-rich metal, the oxygen fugacity is set by the reaction

$$Fe_{metal} + \frac{1}{2}O_2 \Longleftrightarrow FeO_{melt} \quad (1)$$

Such reactions can occur at any depth, and associated pressure and temperature, where metal and silicate equilibrate, but considerations from dynamic models and from siderophile elements establish that the mean pressure of metal–silicate equilibration in the early Earth was high (>25 GPa) (Li and Agee, 1996; Rubie et al., 2003, 2011; Chabot et al., 2005; Rubie et al., 2011; Rubie and Jacobson, 2015). Meanwhile, silicate melts and overlying atmosphere react at low pressure and the oxygen fugacity may be different at high and low pressure if the magma ocean is well mixed and has a similar $Fe^{3+}/\Sigma Fe$ over a range of depths (Hirschmann, 2012). Righter and Ghiorso (2012a) also noted that the pressure of metal–silicate equilibration can influence oxygen fugacities.

1.1. Previous studies on the effect of pressure on $Fe^{3+}/\Sigma Fe$ ratio in silicate melts

Studies focused on 1 bar relations have elucidated the combined effects of fO_2, temperature, and silicate melt composition on the $Fe^{3+}/\Sigma Fe$ ratio of both natural and synthetic silicate liquids (Sack et al., 1980; Kilinc et al., 1983; Kress and Carmichael, 1988; Helgason et al., 1989; Jayasuriya et al., 2004; Partzsch et al., 2004; Borisov and McCammon, 2010). The effect of pressure has been investigated chiefly through low pressure measurements of FeO and Fe_2O_3 volumetric properties (Lange and Carmichael, 1987; Rivers and Carmichael, 1987; Dingwell et al., 1988; Kress and Carmichael, 1991). Direct studies of the effect of pressure include determinations of $Fe^{3+}/\Sigma Fe$ ratios of silicate glasses quenched from high pressure experiments (Mysen and Virgo, 1985; O'Neill et al., 2006).

Measurements of partial molar volumes, thermal expansivities, and compressibilities at 100 kPa (Lange and Carmichael, 1987; Rivers and Carmichael, 1987; Kress and Carmichael, 1991) allow calculation of the influence of pressure on the fO_2 of magmas with fixed $Fe^{3+}/\Sigma Fe$ ratio (Kress and Carmichael, 1991). Owing to a smaller molar volume/atom of FeO compared to Fe_2O_3, compression stabilizes FeO, resulting in higher fO_2 at fixed $Fe^{3+}/\Sigma Fe$ ratio. The same, of course, is true for oxide-oxide or metal-oxide buffers such as QFM or iron-wüstite (IW), but the effect is more pronounced in melts, such that a basalt with fixed $Fe^{3+}/\Sigma Fe$ ratio becomes more oxidized relative to QFM or IW with increased pressure (Kress and Carmichael, 1991).

Mysen and Virgo (1985) performed experiments up to 4 GPa and found $Fe^{3+}/\Sigma Fe$ ratios in Na_2O-FeO-Fe_2O_3-SiO_2 liquids to diminish dramatically with increasing pressure according to a trend that is far greater than that predicted by the thermodynamically-derived model of Kress and Carmichael (1991). However, oxygen fugacity was not buffered in these experiments. O'Neill et al. (2006) quenched glasses from andesitic melts annealed at 1400 °C and 0.4–3 GPa, buffered by the coexistence of Ru and RuO_2 (O'Neill and Nell, 1997) and observed decreasing $Fe^{3+}/\Sigma Fe$, from 0.80 ± 0.03 down to 0.71 ± 0.03 with increasing pressure. They coupled their results to the

1 bar relationship calibrated by Jayasuriya et al. (2004) to formulate an equation of state that predicts a pressure dependence to $Fe^{3+}/\Sigma Fe$ ratio that is qualitatively similar to the model formulated by Kress and Carmichael (1991).

The effect of pressure on $Fe^{3+}/\Sigma Fe$-fO_2 relations in silicate melts is linked to the coordination of Fe^{2+} and Fe^{3+} ions. For mafic silicate melts at low pressure (up to 0.5 GPa) , the average coordination of Fe^{2+} is usually close to 5 (Wilke et al., 2005, 2006, 2007) and for the andesitic glass investigated in this study, XANES and Mössbauer spectroscopy suggest that it is near 5.5 (Zhang et al., 2016). Fe^{3+} apparently takes on multiple coordination states at low pressure, with 4 being most common, but some evidence for 5 and 6 as well (Wilke et al., 2006; Giuli et al., 2011) and for the andesite composition investigated here, Mössbauer and XANES investigations are consistent with average coordination close to 5 (Zhang et al., 2016). With increasing pressure, more highly coordinated geometries are favored. For example, *in situ* X-ray diffraction of molten fayalite shows that mean coordination of Fe^{2+} increases from 4.2 ± 0.2 at ambient pressure to 7.2 ± 0.3 at 7.5 GPa (Sanloup et al., 2013). Pressure should also favor increases in Fe^{3+} coordination, as the partial molar volume of VI-coordinated Fe^{3+} in silicate melts is 25% smaller than that of IV Fe^{3+} (Liu and Lange, 2006). We are not aware of any *in situ* studies pertaining to the coordination of Fe^{3+} in high pressure melts, but Mössbauer investigations of Na_2O-Fe_2O_3-SiO_2 glasses quenched from 0 to 4 GPa may be consistent with gradual increases in Fe^{3+} coordination (Brearly, 1990). However, the changes also may be attributable to shifts in bond angles, similar to those that are chiefly responsible for the anelastic compression effects observed for (MAS, CAS) glasses (Allwardt et al., 2005). At pressures beginning around 8–10 GPa, Fe^{3+} is stabilized in high coordination environments in minerals such as garnet, wadsleyite, and bridgmanite (O'Neill et al., 1993; McCammon, 1997; Frost et al., 2004; Rohrbach et al., 2007), which lead Hirschmann (2012) to speculate that this may also occur in silicate melts.

To further understand the influence of pressure on the relationship between $Fe^{3+}/\Sigma Fe$ ratio and oxygen fugacity, we have quenched glasses from a range of pressures up to 7 GPa and analyzed them by Mössbauer and XANES spectroscopy. We apply the results to understanding gradients in oxygen fugacity in a well-mixed column of magma and the consequences for the compositions and masses atmospheres associated with magma oceans on terrestrial planets.

1.2. Effect of quenching on observed $Fe^{3+}/\Sigma Fe$ ratios and glass structure

An important question is whether the glasses quenched under experimental conditions record the $Fe^{3+}/\Sigma Fe$ ratios and melt structures established at high temperature and high pressure. Many studies have documented the comparatively rapid migration of redox fronts through amorphous silicates exposed to strong gradients in oxygen fugacity (e.g., Cooper et al., 1996; Gaillard et al., 2002, 2003a,b). However, these considerations likely do not apply to the present experiments because (a) the quenching rate is too high and because, (b) unlike quenching at 100 kPa, the mechanism of quench in high pressure experiments does not involve exposure to a gradient in fO_2.

The quench rates in the piston cylinder and multianvil devices at Minnesota range from 125 K/s to 340 K/s, resulting in cooling through the glass transition (~1000 K, Neuville et al., 1993) in 2–6 s (Fig. 1). These are comparable to the fastest cooling rate imposed by Dyar et al. (1987), who observed no measurable differences in $Fe^{3+}/\Sigma Fe$ ratios

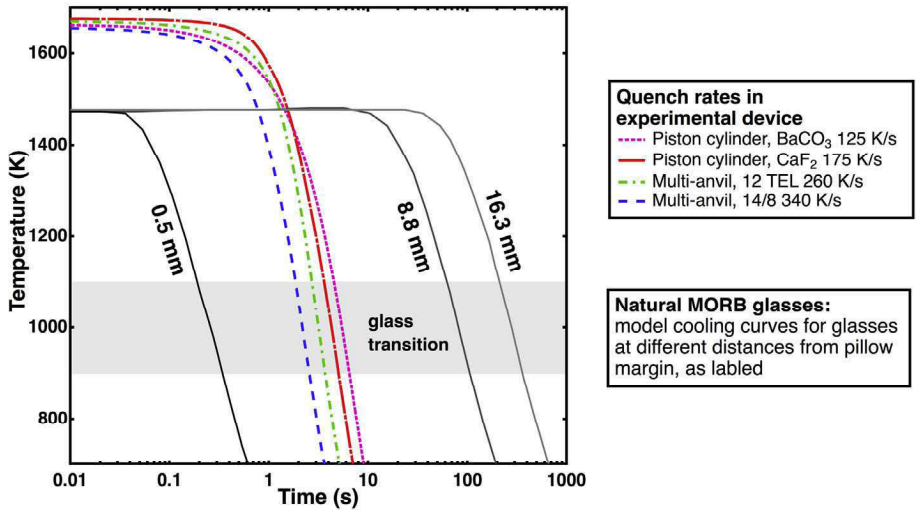

Fig. 1. Temperature–time relations recorded at the thermocouple during quenching for the solid media devices at the University of Minnesota. Mean quench rates are 340 °C/s (multianvil 14/8 assembly), 260 °C/s (multianvil 18/12 assembly), 175 °C/s (piston cylinder, CaF_2 pressure cell), and 125 °C/s (piston cylinder, $BaCO_3$ cell). Data acquired at 8.7 and 3 Hz from the piston cylinder and multianvil, respectively. Also shown are the modeled cooling rates for glasses quenched at different distances from the margin of a natural MORB pillow (Cottrell and Kelley, 2011). Measured $Fe^{3+}/\Sigma Fe$ do not vary in these glasses, indicating that quench rate does not affect ferrous/ferric ratios for cooling rates both faster and slower than those in the experimental apparatuses.

for basalt or andesite quenched from 100 kPa furnaces at rates of 300 K/s and 70 K/s. The quench rates in the present study are also more rapid than the range (150 K/s, >2.5 K/s and <0.02 K/s) imposed by Wilke et al. (2002) across the glass transition for a hydrous Fe-bearing "haplotonalite". They observed shifts in $Fe^{3+}/\Sigma Fe$ ratio only for the slowest quenching rate explored, suggesting that $Fe^{3+}/\Sigma Fe$ ratio is preserved during quenching (>2.5 K/s) that is comparatively slow compared to the present study. We note, however, the experiments of Wilke et al. (2002) were not buffered, and it is not clear whether variations in $Fe^{3+}/\Sigma Fe$ ratio between samples are owing to cooling rates or other effects. Finally, Cottrell and Kelley (2011) found that the $Fe^{3+}/\Sigma Fe$ of glasses remained constant at different distances from the margin of MORB pillow, even though calculated cooling rates varied from >2000 K/s to <2.5 K/s (Fig. 1). Comparison of the cooling rates that occurred in this natural experiment to those in our experimental apparatus supports the inference that the $Fe^{3+}/\Sigma Fe$ of experimental glasses were unaffected by quench.

A related question is whether the structural features of the quenched glass, such as the coordination state of the Fe^{2+} and Fe^{3+} ions, represent those present in the liquid. Indeed, some features of high pressure liquids are not quenched in recovered glasses (Williams and Jeanloz, 1988), but those chiefly responsible for melt densification, such as metal–oxygen coordination and bond angles, may be preserved (Allwardt et al., 2005). Judging from Mössbauer center shifts and quadrupole splittings, Dyar et al. (1987) found no appreciable structural differences in Fe^{2+} and Fe^{3+} environments between andesitic glasses quenched at 300 and 70 K/s, but did detect differences for a third glass quenched at a slower, poorly quantified rate. Wilke et al. (2002) and Rossano et al. (2008) found similar center shifts and quadrupole splittings for haplotonalite glasses quenched rapidly and slowly, but observed considerable line narrowing for those quenched at <0.02 K/s, likely owing to formation of nanocrystalline Fe-oxides (Wilke et al., 2006). Thus, some structural features of rapidly quenched glasses may be indicative of high temperature high pressure melt structure, but such features should be interpreted with care.

Studies showing rapid changes in $Fe^{3+}/\Sigma Fe$ ratio in silicate melts (Cooper et al., 1996; Gaillard et al., 2002; Gaillard et al., 2003a; Gaillard et al., 2003b), invariably involve exposing the melt to a strong redox gradient. This is also true for studies of $Fe^{3+}/\Sigma Fe$ ratio changes on quench when the experiments are conducted at ambient pressure, such as melts dropped from 100 kPa furnaces into air, gas ($Ar\text{-}H_2$), or a brine (e.g., Dyar et al., 1987). Large redox gradients are not present during quenching from high pressure solid media apparatuses, as cooling occurs in a nearly isochemical environment by conduction to the large thermal mass of water-cooled carbide. Even if such gradients were imposed on the experimental charge, their penetration into the melts would be minimal at the quench rates of solid media devices. For example, the most rapid diffusion is associated with the migration of hydrogen, which according to the rate law of Gaillard et al. (2003b) should penetrate less than 1 micron at 1400 °C over the 3–8 s required to cool through the glass transition (~725 °C, Ryan and Sammis, 1981) in multianvil or piston cylinder devices (Fig. 1). We conclude that quench modification of $Fe^{3+}/\Sigma Fe$ ratio owing to reaction with the surrounding environment is not likely to be relevant to glasses quenched in solid media devices.

$Fe^{3+}/\Sigma Fe$ ratios of quenched glasses may differ from those of their precursor liquids if redox reactions with other dissolved heterovalent species occur during cooling through the glass transition. For example, Berry et al. (2006) found that Cr^{2+} present in basaltic melts oxidized to Cr^{3+} during quenching owing to a reaction between Cr and Fe ions, $Cr^{2+}+Fe^{3+} \rightarrow Cr^{3+}+Fe^{2+}$ and such reactions would therefore affect $Fe^{3+}/\Sigma Fe$ ratios of glasses. This problem should be considered carefully if materials contain appreciable concentrations of elements (e.g., Cr, V, Mn, S) that may change valence over the span of oxidation states to be investigated, but these were excluded from our starting materials. Some amount of C in experimental glasses is unavoidable, but we do not expect this to pose a problem because changes in valence of dissolved C occur only under conditions at or below stabilization of graphite (e.g., Stanley et al., 2014), which are much more reducing than the oxidizing conditions in the present study.

2. METHODS

The starting material for this project consists of a synthetic andesite composition similar to that used by O'Neill et al. (2006) and identical to that characterized at 100 kPa by Zhang et al. (2016), and was prepared from reagent oxides (SiO_2, Al_2O_3, Fe_2O_3, TiO_2, MgO), silicates ($CaSiO_3$, Na_2SiO_3) and $KAlSi_3O_8$ composition glass. The Fe_2O_3 consisted of 70% normal reagent oxide and 30% $^{57}Fe_2O_3$ (Isoflex, Inc). Prior to weighing, the SiO_2, Al_2O_3, TiO_2, and MgO were devolatilized by heating at 1000 °C overnight, until the weight stabilized. These reagents were then weighed and mixed by grinding in an agate mortar and pestle under ethanol for at least one hour until the grinding sound ceased and then again devolatilized by firing at 1000 °C for 48 h. Finally, the Fe_2O_3 sources, which had been dried at 800 °C for 1 h and then weighed, were mixed by grinding under ethanol. All the starting materials were stored in a vacuum oven.

Experiments were conducted in 2 or 3 mm diameter Pt capsules, which were sealed by welding (Table 1). All capsules were packed with 80% silicate starting material and 20% of a mixture consisting of equal proportions Ru and RuO_2 and loaded as layers on both the bottom and top of the capsule, producing a sandwich arrangement (Fig. 2). Coexisting Ru and RuO_2 in direct contact with the silicate melt is a highly advantageous buffer for high pressure experiments. It imposes conditions close to that of the magnetite/hematite buffer (O'Neill and Nell, 1997), which is sufficiently oxidizing that loss of Fe to the Pt capsule is negligible and that the Fe^{3+} and Fe^{2+} are both in sufficient abundance for high precision analysis. In contrast to double capsule techniques, it does not require a high H_2O fugacity, and chemical reaction between the buffer phases and silicate melt is negligible (<100 ppm Ru dissolves in

Table 1
Experimental conditions.

Experimental no.	T (°C)	P (GPa)	D (hrs)	Thermo-couple type	Capsule diameter	Pressure apparatus	Iron valence in starting material
Time series							
A839	1400	1.5	1	D	3	PC[*]	3+
A840	1400	1.5	4	D	3	PC	3+
A841	1400	1.5	24	D	3	PC	3+
A843	1400	1.5	24	D	3	PC	2+
A844	1400	1.5	4	D	3	PC	2+
A846	1400	1.5	1	D	3	PC	2+
A848	1400	1.5	24	D	3	PC	2+
A853	1400	1.5	12.5	D	3	PC	3+
A855	1400	1.5	24	D	3	PC	3+
A857	1400	1.5	0.167	D	3	PC	3+
A860	1400	1.5	0.167	D	3	PC	2+
A862	1400	1.5	0.167	D	3	PC	3+
A863	1400	1.5	12	D	3	PC	2+
Variable pressure series							
A867	1500	1.5	4	D	2	PC	3+
A888	1400	3	4	D	2	PC	3+
A896	1400	2	4	D	2	PC	3+
A944	1500	3	4	D	2	PC	3+
A945	1500	2	4	D	2	PC	3+
A952	1500	2.5	4	D	2	PC	3+
B388	1400	2.5	4	D	2	PC	3+
B402	1400	1.5	4	D	2	PC	3+
M535	1600	4	4	D	2	MA[#]	3+
M537	1600	5	4	D	2	MA	3+
M540	1600	3	4	D	2	MA	3+
M543	1600	4.5	4	D	2	MA	3+
M544	1600	3.5	4	D	2	MA	3+
M559	1750	7	0.2	D	2	MA	3+
M562	1750	6	0.2	D	2	MA	3+
M563	1750	5	0.2	D	2	MA	3+
M572	1750	6.5	0.2	D	2	MA	3+
M601	1750	5.5	0.2	B	2	MA	3+
VF1	1400	0.0001	4	S	2	VF[&]	3+

[*] PC: piston cylinder.
[#] MA: multi anvil.
[&] VF: vertical furnace.

glasses, O'Neill et al., 2006). To our knowledge, no other available buffer has these properties.

2.1. Experimental apparatus

A single experiment (VF1) using a sealed 2 mm Pt capsule with $Ru + RuO_2$ buffer at top and bottom was conducted at 100 kPa in a Deltech VT28 vertical gas mixing furnace at 1400 °C, as measured by a Type S ($Pt_{90}Rh_{10}$/Pt_{100}) thermocouple, and lasting 4 h (Table 1). Temperature uncertainties are believed to be ±5 °C based on calibration against Au melting, which was observed at a thermocouple reading of 1059 °C. The VF1 glass was quenched by being put into cold water within seconds.

Experiments up to 3 GPa were performed in a half-inch, end-loaded piston cylinder (PC) apparatus, using the assembly and the temperature and pressure calibrations documented by Xirouchakis et al. (2001). Temperature was measured by Type B ($Pt_{70}Rh_{30}$/$Pt_{94}Rh_6$) or Type D ($W_{97}Re_3$/$W_{75}Re_{25}$) thermocouples (Table 1). Experiments from 3.5 to 7 GPa were performed in a 1000-ton Walker-style multi-anvil device (MA) with an 18/12 (octahedral edge length/WC truncation edge length) assembly described in Dasgupta et al. (2004) and using the 1400–1700 °C calibration presented by Zhang and Hirschmann (2016). Temperature was controlled with a Type D ($W_{97}Re_3$/$W_{75}Re_{25}$) thermocouple positioned immediately above the capsule and oriented axially with respect to the heater. Pressure uncertainties are believed to be ±0.3 GPa, and temperature uncertainties are believed to be ±20 °C (Tenner et al., 2012). Several glass chips from each experiment were removed and double-sided polished for optical examination, XANES, and electron microprobe analyses, while the remainder was ground to powder and mixed with sugar for Mössbauer spectroscopy.

Previous investigations of the approach to Fe^{2+}-Fe^{3+} equilibrium in silicate liquids includes the study of Thornber et al. (1980) and Kilinc et al. (1983) who showed that 5 h is sufficient for the $Fe^{3+}/\Sigma Fe$ ratio to reach steady state at 1200 °C for a basalt and 1350 °C for an andesite, respectively. Five hours was also sufficient for $Fe^{3+}/\Sigma Fe$ ratio in supercooled melts of a pyroxene composition to

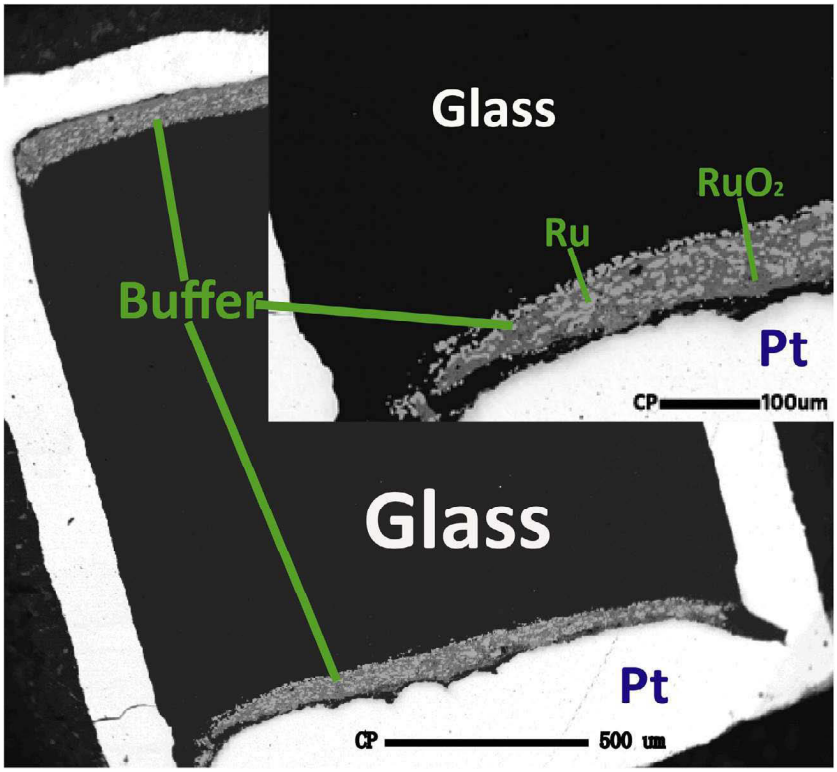

Fig. 2. Back-scattered electron image of experiment M537, which was performed at 5 GPa, 1600 °C, showing that both buffer phases, Ru and RuO_2, coexist with homogeneous crystal-free andesite glass in a Pt capsule. All other samples have same similar textures.

reach steady-state at 650 ± 50 °C (Magnien et al., 2004). We note that establishment of redox equilibrium requires the time for the buffering phases to impose a steady equilibrium fO_2 throughout the experimental charge, as well as the time to achieve homogeneous equilibrium in the melt. To determine appropriate experimental times for our specific composition with the Ru + RuO_2 buffer, we conducted a time series of reversal experiments at 1400 °C and 1.5 GPa (Table 1). In addition to the starting mixture, for which all Fe is initially Fe^{3+}, we also employed a reduced version in which the initial Fe was nearly entirely Fe^{2+}. This latter mixture was prepared in a 100 kPa gas mixing horizontal furnace in an Fe doped Pt crucible with CO_2/CO at QFM-1, 1000 °C for 12 h. As shown in Fig. 3, the $Fe^{3+}/\Sigma Fe$ ratio of the quenched glass converges to a constant ratio after 1 h and for the oxidized starting mix, much of the approach to the equilibrium composition occurs within 10 min. Based on this result, we conducted experiments between 1400 and 1600 °C for 4 h. In order to avoid multi-anvil failures, experiments at 1750 °C were conducted for only 12 min, but considering the much faster reaction expected at hotter conditions and the results from 10 min at 1400 °C (Fig. 3) the high temperature experiments likely also approached equilibrium.

2.2. Analytical methods

2.2.1. XRD and electron microprobe

Quenched glasses were examined by powder X-ray diffraction (XRD) to verify that they consisted only of amorphous silicate. Experimental textures were also examined by back-scattered electron (BSE) and secondary electron imaging (SEI) on using the JEOL JXA8900R EMPA at the University of Minnesota according to procedures detailed in Zhang et al. (2015). Major element concentrations of quenched glasses were determined by wavelength-dispersive EMPA and listed in Table S1. MPI-DING glass, ATHO-G (Jochum et al., 2006) and USGS glasses BCR-2G and BIR-1G (Jochum et al., 2005) were analyzed as secondary standards before and after each sample analysis session, as well as interspersed between each 4 or 5 samples individual sample analyses; this procedure ensured that the electron beam was stable. The intensity data of standards, secondary standards and unknown samples were checked for time dependent intensity (TDI) changes and values for Si kα and Na kα were corrected using a self-calibrated function; no TDI effect was detected for other elements.

2.2.2. Mössbauer spectroscopy

Mössbauer spectra were collected using a constant acceleration Ranger spectrometer at the Institute for Rock Magnetism, University of Minnesota, and the measurements were carried out with a ^{57}Co/Rh source and a pure Fe foil calibrant at room temperature (293 K). Data were collected over 512 channels, which were then folded to produce 256 unique channels. All spectra were collected over at least one day and until sufficient (>1,000,000) counts/channel were accumulated to minimize statistical error. Sample mounts consisted of powdered glass mixed with powdered

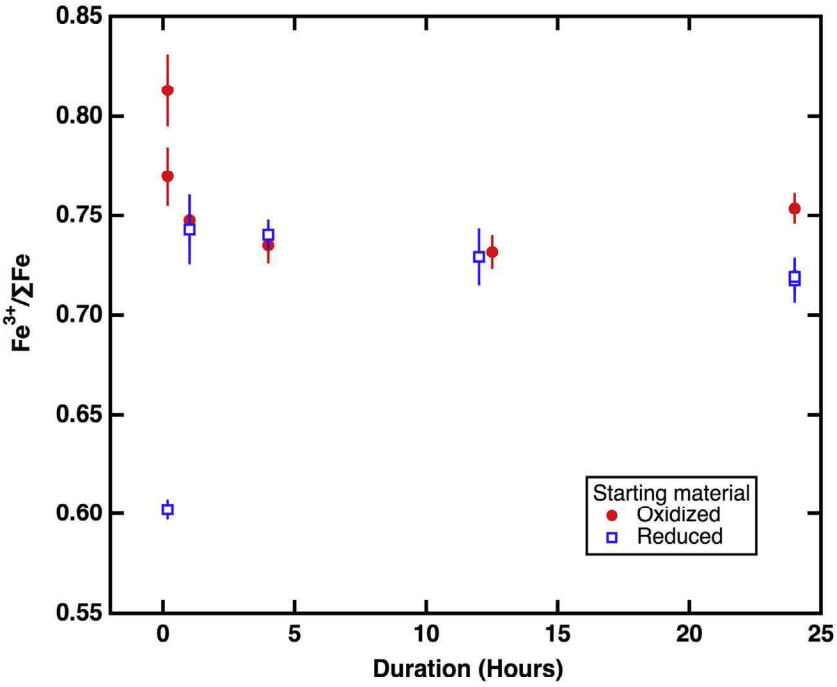

Fig. 3. $Fe^{3+}/\Sigma Fe$ ratios obtained from room temperature Mössbauer spectra of the time series experiments (Table 1) as a function of experimental duration. Red dots and blue squares refer, respectively, to starting materials consisting of an oxide mixture containing pure ferric iron and the same mixture, but reduced in a CO-CO_2 gas stream at IW + 1, 1000 °C for 12 h. (For interpretation of the references to colour in this figure legend, the reader is referred to the web version of this article.)

sugar evenly distributed in an approximately circular shape of diameter 12.7 mm. The absorber thickness was adjusted for an absorber density of ~2 mg/cm^2 Fe.

All spectra have broadened line-shapes typical of silicate glasses and were fitted using distribution methods (Alberto et al., 1996; Rossano et al., 1999, 2008; O'Neill et al., 2006; Borisov and McCammon, 2010; Zhang et al., 2015). All Mössbauer spectra were fitted with a 2D distribution Extended Voigt based fitting (xVBF) method with the RECOIL software package (Lagarec and Rancourt, 1997) and hyperfine parameters with their 1σ uncertainties are listed in Tables S2, S3, and S4.

Most of the spectra consist chiefly of two quadrupole doublets, one each originating from paramagnetic ferric and ferrous iron. For those spectra (like Fig. 4a), there is no obvious evidence of sextets at 12 mm/s. Thus, the Fe ions in those glasses are dominated by paramagnetic Fe^{2+} and Fe^{3+} and the fit process is the same as that described in Zhang et al. (2015). The fitting parameters for each spectrum consisted of the center shift (CS), the quadrupole splitting (QS), and their respective Gaussian widths, σ_{CS} and σ_{QS} (Table S4). Ferric σ_{CS} and the correlation between the σ_{CS} and σ_{QS} (ρ) are assumed to be 0, because the analysis of Alberto et al. (1996) showed that these should be effectively negligible for Fe^{3+} in silicate glasses in low concentrations (5 ~ 15 wt.% Fe_2O_3). The fit of the Fe^{2+} paramagnetic component considers these correlations.

In addition to the doublets, some of the spectra also have nonparamagnetic features. The spectra of 4 of 32 glasses' include an obvious sextet (Fig. 4b). Such sextets are commonly present in quenched mafic glasses (Jayasuriya et al., 2004; O'Neill et al., 2006; Borisov and McCammon, 2010) and are indicative of a ferromagnetic component. Therefore, for fitting these features, we included additional CS and QS parameters as well as that for the hyperfine magnetic field (H) and its Gaussian width (σ_H) (Tables S3 and S4). The, spectra for 14 of the 32 glasses display a broadened magnetic absorption (Fig. 4c and d), which could be owing to a superparamagnetic component observed previously in similar glasses based on magnetic susceptibility measurements (Zhang et al., 2015). For those samples, both 12 mm/s and 20 mm/s scale Mössbauer spectra were collected to ensure full accounting for all Fe components in the quenched material (Fig. S1). All of these spectra were fit in two ways: In the first, we fit the magnetic site with a CS value, its Gaussian width (σ_{CS}), QS and the strength of the hyperfine magnetic field (H) (Figs 4c, S1a S1c, and Table S2). In the second, the sextets were fit using values for the CS, QS, hyperfine magnetic field (H) and its Gaussian width (σ_H) (Figs. 4d, S1b, S1d, and Table S3). Resulting $Fe^{3+}/\Sigma Fe$ ratios for glasses from the time series (Tables S2 and S3) do not depend on the velocity scales used to collect their spectra. We can use these glasses to monitor the influence of the magnetic site on the fits by plotting the resulting $Fe^{3+}/\Sigma Fe$ on the area proportion of each spectrum that is in the magnetic sub-site (P_M). When $P_M < 35\%$, the fit results are consistent between the two fit methods, but where P_M is >35%, the difference between two fit methods is noticeable (Fig. S2). None of the glasses from the variable pressure series, have P_M fractions >35% and we chose the second fitting method (Table S4).

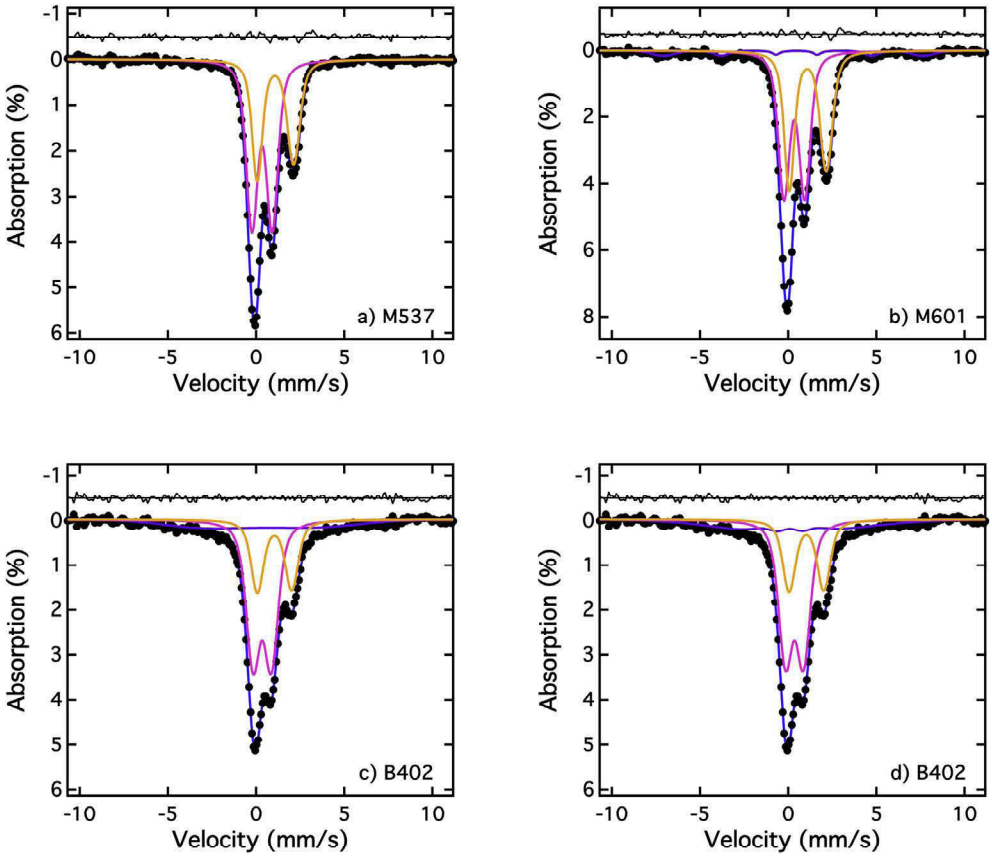

Fig. 4. Examples of Mössbauer spectra and their fits. (a) M537 fitted with only paramagnetic sites (b) M601 fitted with paramagnetic sites and a magnetic sextet site; (c) B402 fitted with paramagnetic sites and a broadened magnetic site; (d) B402 fitted with paramagnetic sites and a magnetic sextet site. For all spectra, the pink curves refer to the paramagnetic Fe^{3+} doublets, the orange curves refer to the paramagnetic Fe^{2+} doublets, and the blue curves are the superposition of all the sites. For (b), (c) and (d), the purple curves refer to the magnetic site. (For interpretation of the references to colour in this figure legend, the reader is referred to the web version of this article.)

2.2.3. X-ray absorption near edge structure (XANES)

Fe K-edge XANES spectra of glass chips were collected at station X26A of the National Synchrotron Light Source (NSLS), Brookhaven National Lab (BNL) using a 9×5 μm spot and at beamline 13-IDE at the Advanced Photon Source (APS), Argonne National Lab (ANL) using 2×2 μm or 25×25 μm spots. A minimum of 3 spectra were collected on each andesitic glass. All spectra were collected in fluorescence mode. 7112 eV and 7110.7 eV were specified as the first derivative peak for Fe foil at NSLS and APS, respectively, which defined the energy calibration for the system. Spectra were recorded with four energy regions previously defined by Cottrell et al. (2009) and Zhang et al. (2016) for NSLS and APS, respectively. Because the monochromated beam energy can drift with time, and in order to facilitate comparison of spectra collected at X26A with spectra collected at 13-ID-E, we normalized of all spectra to the standard glass LW_0 assuming a centroid energy of 7112.3 eV (Cottrell et al., 2009). We collected spectra on LW_0 at variable time intervals dependent upon the stability and drift of the monochromated energy. The precision of centroid energy is 0.008 ± 0.005 eV, and for the basalt calibration with 13 reference glasses, the precision of $Fe^{3+}/\Sigma Fe$ is ± 0.0068 (Cottrell et al., 2009). A more complete account of spectral collection and fitting details is given in Zhang et al. (2016). All corrected parameters resolved from fits are listed in Table S5.

3. RESULTS

3.1. Textures and major element compositions of glasses

XRD patterns suggest that the quenched material is amorphous, and that silicate crystals are absent. The Ru + RuO_2 buffer assemblage was evident at the top and bottom of each capsule (Fig. 2). Electron microprobe analyses indicate all quenched glasses have similar compositions close to that of the original andesite (Table S1).

3.2. $Fe^{3+}/\Sigma Fe$ ratio determinations from Mössbauer spectroscopy

Proportions of Fe^{3+} and Fe^{2+} are calculated from the areas of their sub-spectra, which are listed in Tables S2, S3 and S4. For andesitic glasses of the same compositions as those studied here, Zhang et al. (2015) showed that the relative abundances of Fe^{3+} and Fe^{2+} in quenched andesitic

Table 2
$Fe^{3+}/\Sigma Fe$ ratios determined from Mössbauer spectra collected at room temperature.

No.	$Fe^{3+}/\Sigma Fe$*	C#	Corrected $Fe^{3+}/\Sigma Fe$&
A867	68.80(3.00)	1.14(0.04)#	65.96(3.00)
A888	68.20(0.77)		65.33(0.77)
A896	70.10(0.54)		67.32(0.54)
A944	63.73(0.43)		60.69(0.43)
A945	65.28(0.31)		62.30(0.31)
A952	65.78(0.48)		62.81(0.48)
B388	68.19(0.39)		65.32(0.39)
B402	73.23(3.13)		70.62(3.13)
M535	59.50(0.57)		56.35(0.57)
M537	59.30(0.67)		56.15(0.67)
M540	61.12(0.57)		58.01(0.57)
M543	60.88(0.56)		57.76(0.56)
M544	60.01(0.51)		56.87(0.51)
M559	53.52(0.66)		50.29(0.66)
M562	54.1(0.66)		50.88(0.66)
M563	56.76(0.99)		53.57(0.99)
M572	52.50(0.88)		49.27(0.88)
M601	55.49(0.88)		52.28(0.88)
VF1	75.30(0.63)	1.20(0.06)#	71.76(0.62)

Uncertainties are in one sigma standard deviation (1σ).
* $Fe^{3+}/\Sigma Fe$ obtained from Mössbauer spectra collected at room temperature.
# Correction number from Tables S6, S7, based on Zhang et al. (2015).
& $Fe^{3+}/\Sigma Fe$ corrected with C through equation $(Fe^{3+}/\Sigma Fe)_{corrected} = (Fe^{3+}/\Sigma Fe)/[(Fe^{3+}/\Sigma Fe) + C^*(1 - Fe^{3+}/\Sigma Fe)]$.

glasses must be corrected for the effects of recoilless fractions according to a correction number C, in which the ratio of Fe^{3+} and Fe^{2+} ions in a sample, $N(Fe^{3+})/N(Fe^{2+})$, is related to the areas of the associated paramagnetic doublets $AA(Fe^{3+})/AA(Fe^{2+})$,

$$AA(Fe^{3+})/AA(Fe^{2+}) = C \times N(Fe^{3+})/N(Fe^{2+}). \quad (2)$$

The applicable values of C are 1.14 ± 0.04 and 1.20 ± 0.06 (Tables S6 and S7, based on Zhang et al. (2015), and corrected in Supplementary Materials), respectively, for glass quenched from high and ambient pressures. The difference is presumably owing to different structures and densities of these glasses, and so we apply the former value for all the glasses in this study except for the lone ambient pressure glass, VF1, for which we apply the latter value. The uncorrected and corrected $Fe^{3+}/\Sigma Fe$ ratios of quenched glasses are listed in Table 2.

Values $Fe^{3+}/\Sigma Fe$ ratios of andesitic liquids buffered by Ru-RuO_2 decrease as pressure increases (Fig. 5), as previously observed by O'Neill et al. (2006). At a given pressure, $Fe^{3+}/\Sigma Fe$ decreases with increasing temperature, but this is chiefly because at higher temperature, the Ru/RuO_2 buffer becomes less oxidized compared to Fe-O buffers such as QFM (O'Neill and Nell, 1997).

Three experiments, all at 1400 °C, were performed at the same conditions as experiments by O'Neill et al. (2006) and these allow direct comparison of experimental and analytical results between the two studies. At 1.5 GPa, experiment B402, has the same $Fe^{3+}/\Sigma Fe$ ratio within uncertainty, 73.2 ± 3.1 (Table 2) as the correlative experiment from O'Neill et al. (2006) (73.4 ± 1.0). However those at 2 GPa (A896), and 3 GPa (A888) have slightly different $Fe^{3+}/\Sigma Fe$ ratios from the analogous experiments performed by O'Neill et al. (2006) (70.1 ± 0.5 vs. 72.1 at 2 GPa and 68.2 ± 0.8 vs. 70.8 at 3 GPa, respectively). These differences may

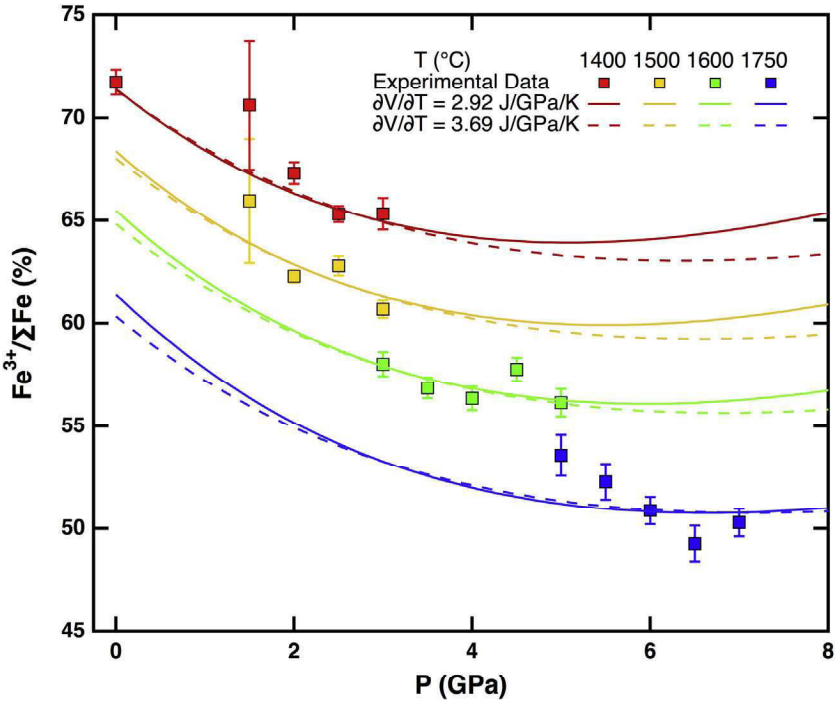

Fig. 5. Effect of pressure on $Fe^{3+}/\Sigma Fe$ of andesitic melts buffered by Ru + RuO_2. Different colors refer to different temperatures. The curves are the thermodynamic fits with Eq. (11), which is based on an ideal silicate solution, and with different $\frac{\partial V}{\partial T}$ values for FeO: 2.92 from Lange and Carmichael (1987) and 3.69 from Guo et al. (2014). Fit coefficients are listed in Table 4.

reflect problems with precision when sextets are present in the spectra, as is the case for all the data from O'Neill et al. (2006), and for B402, but not A896 and A888 (Table S4).

3.3. XANES spectra of andesitic glasses

Features of the Fe Kα XANES pre-edge can be calibrated to give quantitative $Fe^{3+}/\Sigma Fe$ ratios of silicate glasses (Berry et al., 2003; Botcharnikov et al., 2005; Wilke et al., 2005; O'Neill et al., 2006; Cottrell et al., 2009; Cottrell and Kelley, 2011; Dauphas et al., 2014; Zhang et al., 2016), but because the pre-edge also depends on bonding characteristics such as Fe-O coordination (Wilke et al., 2005; Zhang et al., 2016), calibrations based on glasses quenched from low pressure are not necessarily applicable to those quenched from high pressure. Consequently, the XANES spectra collected in this study can be used to infer the effects of pressure on typical bonding environments of Fe^{2+} and Fe^{3+} in quenched andesitic glasses. Relationships between pre-edge spectral features and $Fe^{3+}/\Sigma Fe$ can also be interpreted with the aid of $Fe^{3+}/\Sigma Fe$ determined from Mössbauer spectra as described above.

Deconvolution of the XANES pre-edge into centroids and relative areas of sub-peaks attributable to Fe^{2+} and Fe^{3+} was calculated according to the methods of Cottrell et al. (2009), and fit parameters are listed in Table S5. Spectra for samples collected at both NSLS and APS give the same centroid energies, which are the weighted energies of the entire pre-edge area within 1 sigma standard deviation (Fig. S3, Table S5). For glasses quenched from 1.5 to 7 GPa and $Fe^{3+}/\Sigma Fe$ ratios determined from Mössbauer spectroscopy ranging from 0.49 to 0.72, the averaged Centroid Energy varies from 7113.085 to 7113.338 (Table 3).

Trends of the ratio of pre-edge sub-peak intensities, $I(Fe^{3+})/I(Fe^{2+})$, versus $Fe^{3+}/\Sigma Fe$, determined from Mössbauer spectroscopy, are distinct for high pressure and ambient pressure andesitic glasses (Fig. 6). The high pressure intensity ratios are described by the function

$$\frac{I(Fe^{3+})}{I(Fe^{2+})} = (0.473 \pm 0.958) + (0.0606 \pm 0.0159) \times \left(\frac{Fe^{3+}}{\Sigma Fe} \times 100\right) \quad (3)$$

which considers the uncertainties from intensity ratios and $Fe^{3+}/\Sigma Fe$ ratios.

4. DISCUSSION

4.1. Local environments of Fe^{3+} and Fe^{2+} in silicate glasses

With increasing pressure, shifts in the bonding environments of Fe^{2+} and Fe^{3+} of quenched glasses can be characterized from both Mössbauer spectroscopy and XANES. Quenchable compression mechanisms in silicate glasses include both steric effects and changes in mean cation-oxygen coordination numbers (CN) (Allwardt et al., 2005).

For Mössbauer spectroscopy, the relationship between hyperfine parameters CS and QS and CNs for Fe^{3+} and Fe^{2+} ions is well established for minerals (Dyar et al., 2006), but interpretation for glasses is somewhat more complex, in part because ions can reside in a population of environments, rather than in discrete sites with a unique coordination (Wilke et al., 2005; Zhang et al., 2016). Parameters that describe the Mössbauer spectra of silicate glasses constrain average coordination.

Values of center shifts and quadrupole splittings of Fe^{3+} and Fe^{2+} in andesitic glasses as a function of pressure are shown in Fig. 7. CSs of Fe^{3+} vary little from 1.5 to 7 GPa, with values chiefly near 0.341 ± 0.010 mm/s, though the low pressure (0.1 MPa) glass, VF1, is lower (0.297 ± 0.007). Values of QSs also fail to show a discernable trend, with most near 1.172 mm/s. For Fe^{2+}, CS increases 0.05 mm/s from 1.5 GPa to 5 GPa then is nearly constant at 1.10 mm/s between 5 and 7 GPa, whereas QS increases linearly with pressure up to 7 GPa from 1.820 to 2.213 mm/s. These patterns suggest that for these comparatively oxidized glasses (all with $Fe^{3+}/\Sigma Fe > 0.5$), the average coordination number for Fe^{3+} is close to 5 (Dyar, 1985; Zhang et al., 2016) and changes little from 100 kPa to 7 GPa, but that the average coordination number of Fe^{2+} increases slightly, from between 5 and 6 (Dyar, 1985; Dyar et al., 2006). The marked increase in QS for Fe^{2+}, which is more pronounced than the CS shift, likely suggests that additional compression of Fe^{2+}-O polyhedra occurs owing to changes in O–Fe^{2+}–O bond angles resulting in less-symmetric Fe^{2+} sites.

XANES pre-edge spectra also constrain the effects of pressure on Fe^{2+} and Fe^{3+} site geometries of quenched glasses. Estimates of Fe ion geometries can be calculated from the variogram approach of Wilke et al. (2005), which compares simultaneously the pre-edge centroid positions and integrated intensities to those of minerals with Fe in known oxidation state and CN. As shown in Fig. 8, the diminished integrated intensities with increasing pressure reflect an increase in CN. A similar conclusion can be drawn by comparison between the low integrated intensities of the high pressure glasses and those for andesitic and basaltic glasses quenched from low pressure from Zhang et al. (2016) and Wilke et al. (2005), respectively. Quantitative estimates of mean coordination numbers of Fe^{3+} and Fe^{2+} can be calculated from the approach of Zhang et al. (2016), which combines the XANES pre-edge characteristics with $Fe^{3+}/\Sigma Fe$ determined from Mössbauer analyses (Fig. 9). For the high pressure glasses, mean CN values for Fe^{3+} are 5.3 ± 0.1, with no discernable pressure variation, while the mean coordination number of Fe^{2+} increases from 5.5 to 6.0 over the pressure range explored. Thus, the results from Mössbauer and XANES spectroscopies agree that at modest pressure, compression of Fe^{3+} in andesitic silicate liquid is not accompanied by significant geometric changes, but that Fe^{2+} compression is facilitated by significant increases in mean coordination and, possibly, bond geometries. This latter result is in qualitative agreement though not as pronounced as the CN of Fe^{2+} in fayalite liquid inferred from XRD scattering, Sanloup et al. (2013),

Table 3
Parameters obtained from XANES spectra.

No.	APS				NSLS			
	$I(Fe^{3+}) + I(Fe^{2+})$*	$I(Fe^{3+})/I(Fe^{2+})$*	$I(Fe^{3+})/[I(Fe^{3+}) + I(Fe^{2+})]$*	Centroid Energy (eV)	$I(Fe^{3+}) + I(Fe^{2+})$*	$I(Fe^{3+})/I(Fe^{2+})$*	$I(Fe^{3+})/[I(Fe^{3+}) + I(Fe^{2+})]$*	Centroid energy (eV)
A867	0.1447(0.0055)	4.557(0.378)	0.819(0.013)	7113.205(0.016)	0.1459(0.0011)	4.363(0.394)	0.813(0.014)	7113.238(0.014)
A888	n.a.*				n.a.*			
A896	0.1441(0.0026)	4.493(0.227)	0.818(0.008)	7113.233(0.007)	0.1522(0.0015)	4.250(0.195)	0.809(0.007)	7113.230(0.010)
A944	0.1370(0.0072)	4.038(0.194)	0.801(0.008)	7113.197(0.005)	0.1399(0.0035)	3.656(0.122)	0.785(0.006)	7113.197(0.019)
A945	0.1354(0.0018)	4.270(0.075)	0.810(0.003)	7113.201(0.004)	0.1415(0.0055)	3.677(0.314)	0.785(0.015)	7113.184(0.010)
A952	0.1361(0.0051)	4.343(0.114)	0.813(0.004)	7113.195(0.009)	0.1547(0.0026)	4.057(0.090)	0.802(0.004)	7113.211(0.001)
B388	0.1389(0.0017)	4.763(0.145)	0.826(0.004)	7113.245(0.002)	0.1452(0.0044)	4.111(0.651)	0.802(0.024)	7113.244(0.013)
B402	0.1395(0.0022)	4.779(0.178)	0.827(0.005)	7113.229(0.008)	0.1467(0.0039)	4.211(0.254)	0.808(0.009)	7113.241(0.009)
M535	n.a.*				n.a.*			
M537	0.1360(0.0020)	3.792(0.231)	0.791(0.010)	7113.168(0.006)	n.a.*			
M540	0.1482(0.0050)	3.472(0.358)	0.775(0.018)	7113.143(0.014)	0.1345(0.0031)	2.868(0.183)	0.741(0.012)	7113.116(0.018)
M543	0.1260(0.0031)	3.876(0.043)	0.795(0.002)	7113.162(0.010)	0.1395(0.0007)	3.298(0.205)	0.767(0.011)	7113.137(0.014)
M544	0.1100(0.0053)	2.899(0.881)	0.735(0.059)	7113.165(0.036)	0.1001(0.0022)	2.945(0.348)	0.745(0.022)	7113.198(0.015)
M559	0.1364(0.0061)	4.536(0.573)	0.818(0.020)	7113.194(0.035)	n.a.*			
M562	0.1313(0.0117)	3.715(0.232)	0.787(0.011)	7113.131(0.019)	0.1290(0.0025)	3.681(0.190)	0.786(0.009)	7113.128(0.004)
M563	n.a.*				n.a.*			
M572	0.1114(0.0026)	3.612(0.160)	0.783(0.008)	7113.099(0.007)	0.1132(0.0027)	3.442(0.316)	0.774(0.016)	7113.071(0.009)
M601	0.1179(0.0014)	3.376(0.028)	0.771(0.001)	7113.092(0.005)	n.a.*			
VF1	0.1680(0.0065)	5.137(0.133)	0.837(0.004)	7113.338(0.005)	n.a.*			

Uncertainties are in one sigma standard deviation (1σ)

APS: Advanced Photon Source.
NSLS: National Synchrotron Light Source.
#Results not available.
* Intergrated pre-edge intensity.

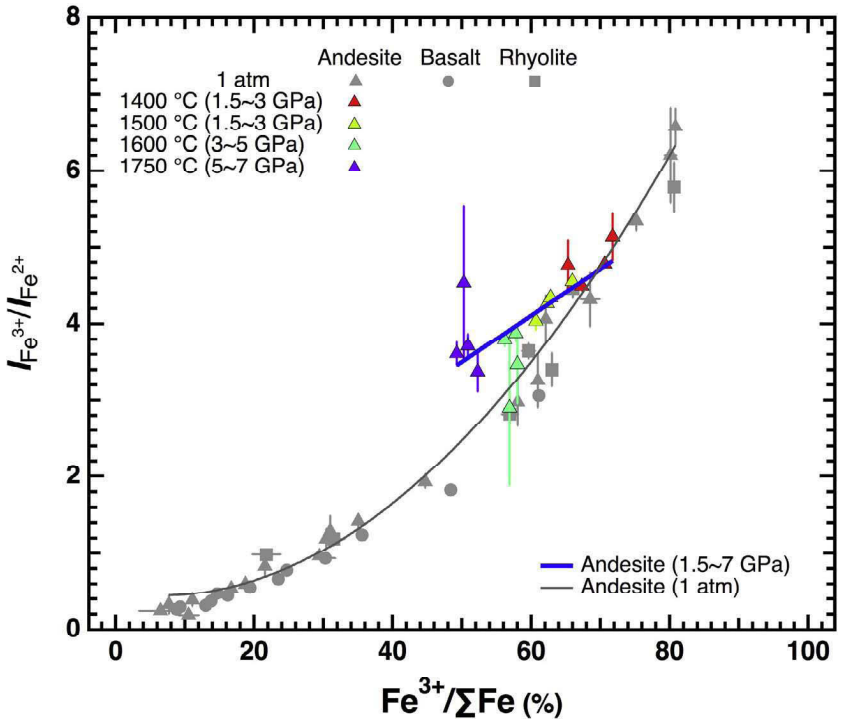

Fig. 6. Integrated XANES pre-edge intensity ratios ($I(Fe^{3+})/I(Fe^{2+})$) vs. $Fe^{3+}/\Sigma Fe$ (%) after Zhang et al. (2016). 100 kPa basalt and rhyolite data are from Cottrell et al. (2009); 100 kPa andesite Intensity ratios from Zhang et al. (2016); and 100 kPa andesite $Fe^{3+}/\Sigma Fe$ ratios from Zhang et al. (2016) and corrected with C = 1.20 (Table S7). Color triangles indicate $I(Fe^{3+})/I(Fe^{2+})$ of glasses synthesized at 1.5–7 GPa acquired only at APS. Data from NSLS are excluded because their intensity ratios are systematically smaller owing to the absence of a dead time correction for the NSLS spectra (Fig. S4, Table S5). Gray curves are the best fit for andesitic glasses synthesized at 100 kPa from Zhang et al. (2016). The blue line is the best fit to the andesite glasses synthesized at 1.5–7 GPa.

which increases from 4.8 to 7.2 from ambient pressure up to 7.5 GPa.

4.2. Effect of pressure on $Fe^{3+}/\Sigma Fe$

The reaction describing homogeneous iron redox equilibrium in a silicate melt is

$$\underset{\text{magma}}{\text{FeO}} + \frac{1}{4}O_2 = \underset{\text{magma}}{\text{FeO}_{1.5}} \quad (4)$$

which is governed by the thermodynamic properties of Fe oxides in silicate melts according to the relation:

$$\frac{-\Delta G^0_{(T,P)}(4)}{RT} = \ln\left(\frac{X^{\text{magma}}_{\text{FeO}_{1.5}}}{X^{\text{magma}}_{\text{FeO}}}\right) + \ln\left(\frac{\gamma^{\text{magma}}_{\text{FeO}_{1.5}}}{\gamma^{\text{magma}}_{\text{FeO}}}\right) - \frac{1}{4}\ln fO_2 \quad (5)$$

where $\Delta G^0_{(T,P)}(4)$ is the free energy change of reaction (4) at the temperature (T) and pressure (P) of interest, and Xs and γs are, respectively, the mole fractions and activity coefficients of the Fe-oxide components, and R is the gas constant. Because the difference in molar partial volumes between $FeO_{1.5}$ and FeO, $\Delta V_{\text{magma}(T,P)}$ is non-zero (Mo et al., 1982; Lange and Carmichael, 1987; Liu and Lange, 2006), this relationship is pressure-dependent and can be expressed as

$$\Delta G^0_{(T,P)}(4) = \Delta G^0_{(T,P_0)}(4) + \int_{P_0}^{P} \Delta \overline{V}_{\text{magma}(T,P)}(4)\mathrm{d}P \quad (6)$$

where $P_0 = 100$ kPa. The $Fe^{3+}/\Sigma Fe$ ratios of glasses described in this paper resolved from Mössbauer spectroscopy are plotted as a function of pressure along different isotherms in Fig. 5. Accounting for the observed changes in $Fe^{3+}/\Sigma Fe$ using Eq. (6) requires first accounting for the fO_2 fixed by the $Ru + RuO_2$ buffer, which changes with pressure and temperature according to the expression:

$$\log_{10} f_{O_2}(Ru - RuO_2) = -\frac{16953}{T} + 17.98 - 2.660\log_{10}T + 562\frac{P}{T} \quad (7)$$

where T is in K and P is in GPa (O'Neill and Nell, 1997).

To model the volumes of Fe-oxides in silicate melts as a function of pressure, we apply the Murnaghan equation of state in the form suggested by Holland and Powell (2001).

$$V_{(T,P)} = V_{(T,P_0)}\left[1 + P\left(\frac{\kappa'}{\kappa}\right)\right]^{-1/\kappa'} \quad (8)$$

where κ is the bulk modulus, and κ' its pressure derivative. We assume a value of 4 for κ'; although this value comes chiefly from its applicability to crystalline oxides and silicates, the available evidence on silicate melts indicates that it is not inappropriate (Rigden et al., 1989; Miller et al., 1991; Campbell et al., 2009). Rearranging and integrating Eqs. (6) and (8) leads to

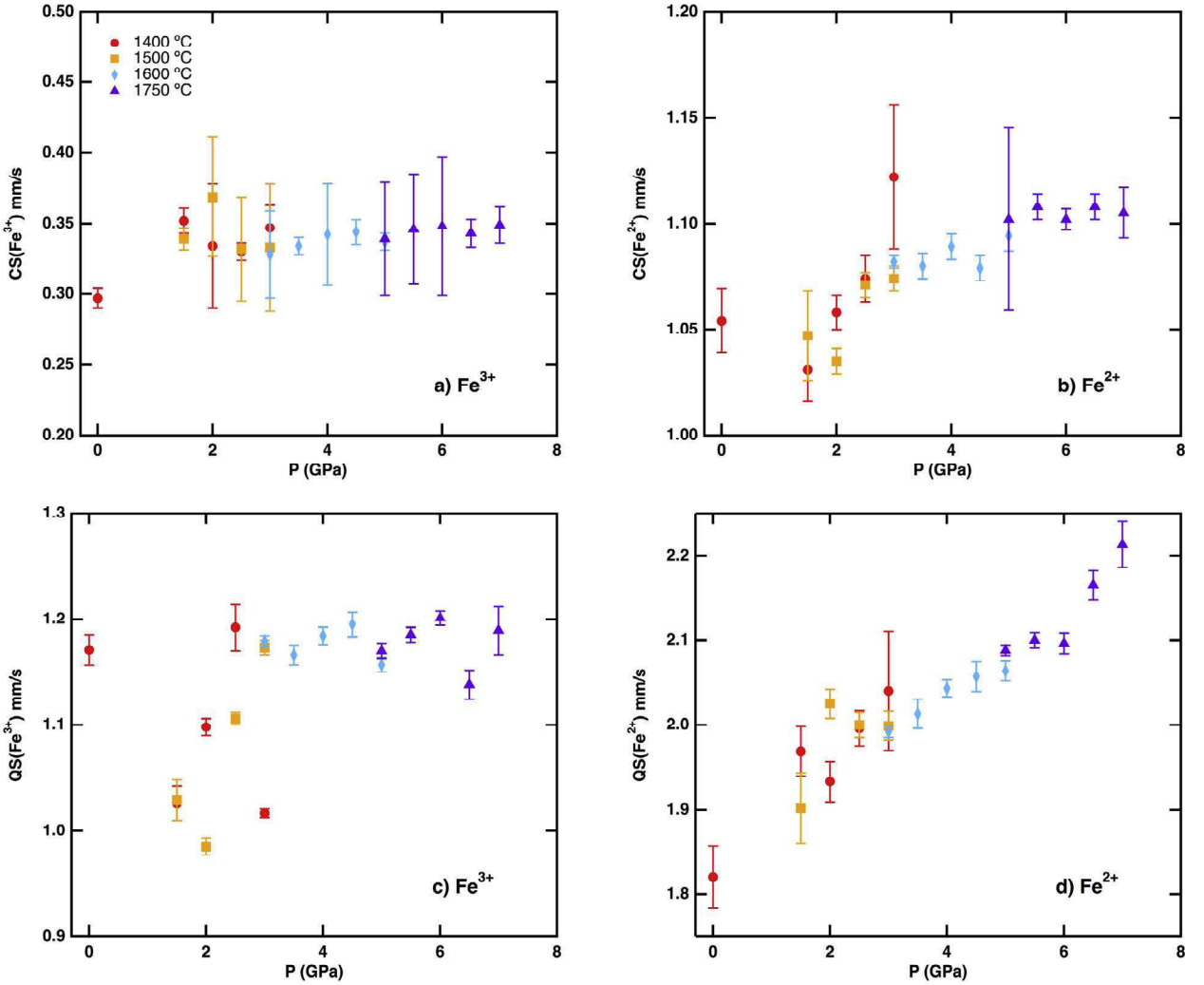

Fig. 7. Changes in Mössbauer hyperfine parameters, center shift (CS) and quadrupole splitting (QS), with pressure up to 7 GPa. For Fe^{3+} (panels a and c), there are no discernable changes in hyperfine parameters with pressure, but for Fe^{2+} CS (panel b) increases with pressure, most notably up to 5 GPa, and QS (panel d) increases nearly linearly across the pressure range.

$$\int_{P_0}^{P} \overline{V}_{(1673\mathrm{K},\ P)}\mathrm{d}P = \frac{\overline{V}_{(1673\mathrm{K},P_0)}\kappa}{\kappa' - 1}\left[\left(1 + \frac{\kappa' P}{\kappa}\right)^{1-1/\kappa'} - 1\right] \quad (9)$$

The spectroscopic results discussed in Section 4.1 indicate that coordination and bonding of ferric iron in andesitic liquids does not change appreciably over the pressures investigated, so applicable equation of state parameters are possibly well-constrained by low pressure measurements. We take the $\overline{V}_{(T,P_0)}$ of $FeO_{1.5}$ in silicate melts to be $[20170 + 4.54(T - 1673)] \times 10^{-9}$ m^3/mol (Lange and Carmichael, 1987) and κ equal to 16.6 GPa (Kress and Carmichael, 1991). Based on measurements of alkali iron silicate liquids, Liu and Lange (2006) give an updated partial molar volume of $FeO_{1.5}$ of 2.0760×10^{-5} m^3/mol, but with a negligible $\frac{\partial V}{\partial T}$, so we choose to retain the older parameters applicable to more complex liquids from Lange and Carmichael (1987). We consider two alternative values of the $\frac{\partial V}{\partial T}$ for FeO, 2.92×10^{-9} m^3/mol/K from Lange and Carmichael (1987) and 3.69×10^{-9} m^3/mol/K from Guo et al. (2014). The values of $\overline{V}_{(T,P_0)}$ and κ for FeO are then fit from the experimental data in Fig. 5. We note that the temperature span of our experiments is insufficient to extract meaningful constraints on the thermal expansion term for Fe^{2+}.

Rearranging Eqs. (5) and (6) yields

$$\ln\left(\frac{X^{\mathrm{magma}}_{\mathrm{FeO_{1.5}}}}{X^{\mathrm{magma}}_{\mathrm{FeO}}}\right) = \frac{1}{4}\ln fO_2 - \ln\left(\frac{\gamma^{\mathrm{magma}}_{\mathrm{FeO_{1.5}}}}{\gamma^{\mathrm{magma}}_{\mathrm{FeO}}}\right) + \frac{-\Delta G^0_{(T,P_0)}(4)}{RT} + \frac{-\int_{P_0}^{P}\Delta\overline{V}_{\mathrm{magma}}(4)\mathrm{d}P}{RT} \quad (10)$$

and we treat $-ln\left(\frac{\gamma^{\mathrm{magma}}_{\mathrm{FeO_{1.5}}}}{\gamma^{\mathrm{magma}}_{\mathrm{FeO}}}\right)$ and $-\Delta G^0_{(T,P_0)}(4)$ as refinable parameters. Using a weighted Levenberg–Marquardt algorithm to values of $\ln\left(\frac{X^{\mathrm{magma}}_{\mathrm{FeO_{1.5}}}}{X^{\mathrm{magma}}_{\mathrm{FeO}}}\right)$ as a function of pressure and temperature produces the relation

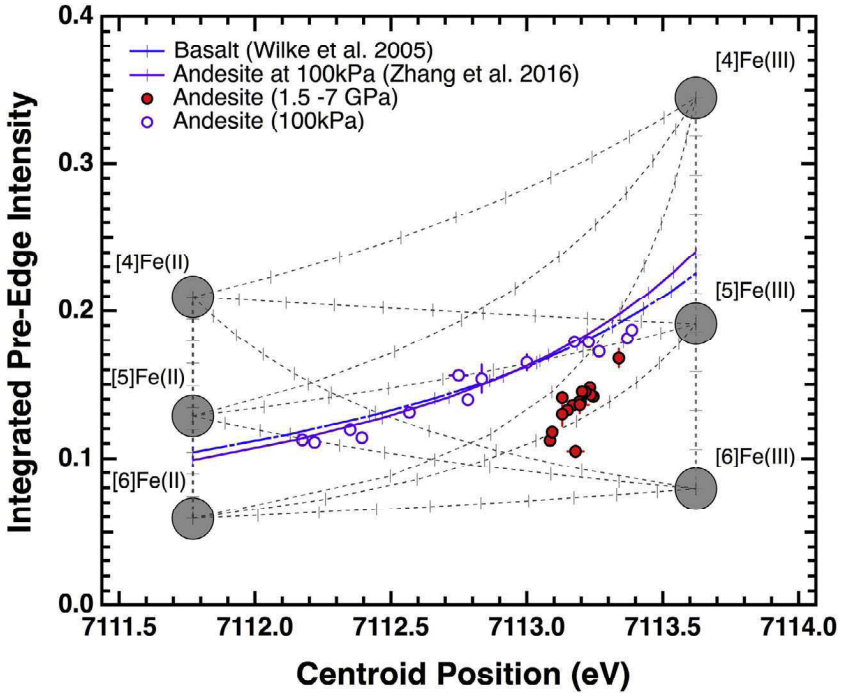

Fig. 8. XANES pre-edge parameters of andesitic glasses synthesized at 1.5–7 GPa plotted on a variogram after Wilke et al. (2001) and Zhang et al. (2016). Gray fields designate pre-edge parameters for the Fe coordination and oxidation state indicated, based on typical values for minerals (Wilke et al., 2001). For andesitic glasses, comparison of high pressure data (this study, red solid circles) with those from 100 kPa (purple empty circles, Zhang et al., 2016) shows that glasses quenched from high pressure have systematically lower pre-edge intensities, indicating higher coordination. Values of $Fe^{3+}/\Sigma Fe$ of the glasses are taken from Mössbauer determinations. Blue dash and purple solid lines between fields indicate the variation of pre-edge parameters of low-pressure glasses assuming binary mixtures of respective end-members' intensity determined by Wilke et al. (2005) for basalt and Zhang et al. (2016) for andesite. Ticks on curves refer to the percentage of mixtures. (For interpretation of the references to colour in this figure legend, the reader is referred to the web version of this article.)

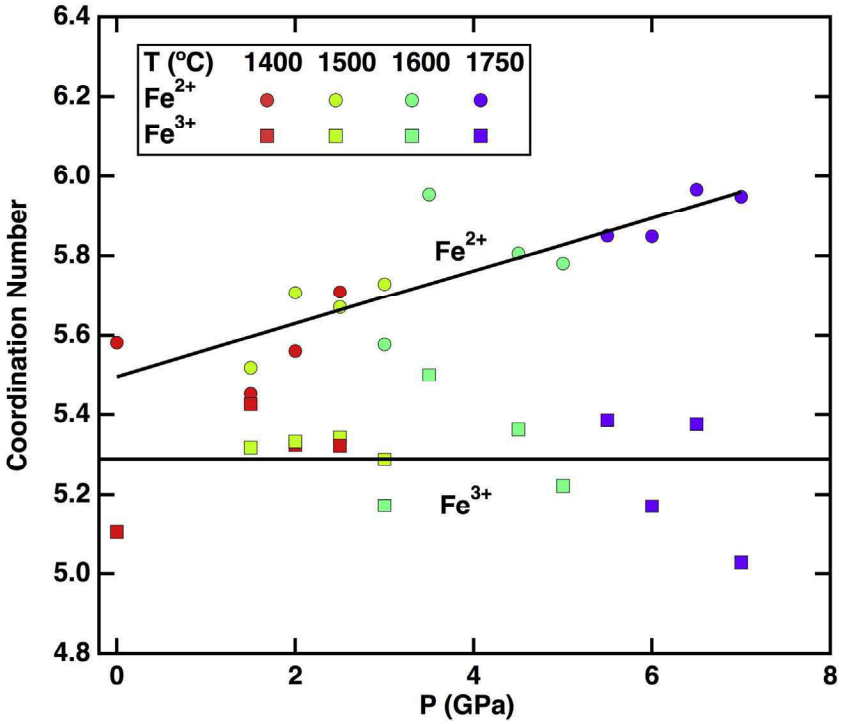

Fig. 9. Coordination numbers (CN) of Fe^{2+} and Fe^{3+} calculated from XANES pre-edge intensities and Mössbauer $Fe^{3+}/\Sigma Fe$ according to the approach detailed in Zhang et al. (2016). With increasing pressure, there are no appreciable changes in the CN of Fe^{3+}, but that for Fe^{2+} changes from about 5.5 to 6 from 100 kPa to 7 GPa.

$$\ln\left(\frac{X_{FeO_{1.5}}^{magma}}{X_{FeO}^{magma}}\right) = \frac{1}{4}\ln fO_2 + \boldsymbol{a} + \frac{\boldsymbol{b}}{RT} - [20170 + 4.54 \times (T - 1673)] \times \frac{16.6}{3} \times \frac{(1 + 0.241P)^{0.75} - 1}{RT} + \left[\boldsymbol{c} + \frac{\partial V}{\partial T} \times (T - 1673)\right] \times \frac{4}{3\boldsymbol{d}} \times \frac{(1 + \boldsymbol{d} \times P)^{0.75} - 1}{RT} \quad (11)$$

Table 4
Thermodynamic fit parameters for Eq. (10).

$\frac{\partial V}{\partial T}$	2.92[#]	3.69[*]
a	−6.376 ± 0.186	−6.627 ± 0.187
b	107,257 ± 2601	110,729 ± 2623
c	15,095 ± 237	15,243 ± 246
d	0.0827 ± 0.0216	0.1137 ± 0.0243
κ[&]	36.61	27.11
κ[@]	30.3[^]	21.1[*]
$\mathbf{X^2}$	32.32	31.29

Uncertainties are in one sigma standard deviation (1σ).
$\frac{\partial V}{\partial T}$: in J/GPa/K.
[#] From Lange and Carmichael (1987).
[*] From Guo et al. (2014).
[&] Bulk modulus, which is calculated using equation κ = 4/d.
[@] Bulk modulus from reference.
[^] From Kress and Carmichael (1991).

The resulting trends of $Fe^{3+}/\Sigma Fe$ ratios are compared to the experimental data in Fig. 5. Similar fit results are obtained from different $\frac{\partial V}{\partial T}$ values (Table 4, Fig. 5), showing the limited constraints on $\frac{\partial V}{\partial T}$.

We note that this thermodynamic fit could be improved with a compositionally dependent model that accounts for non-ideal mixing, a more sophisticated equation of state, and direct constraints on κ′ values for $FeO_{1.5}$ and FeO. But these more advanced considerations cannot be constrained from the limited span of T, P, and $Fe^{3+}/\Sigma Fe$ of the experimental data in Fig. 5. This is particularly so because variations in T, P, and $Fe^{3+}/\Sigma Fe$ in the experimental data are coupled, such that effects of standard state and non-ideal mixing cannot be separated.

4.3. Effect of pressure on the relationship between fO_2 and $Fe^{3+}/\Sigma Fe$ in silicate magmas

The new thermodynamic model (Eqs. (11)) and (S2) can be used to calculate the relationship between $Fe^{3+}/\Sigma Fe$ in melts as function of pressure and fO_2 relative to the IW buffer at 1400 °C (Fig. 10). Such calculations would have qualitatively similar relations relative to any standard metal-oxide buffer, and we choose IW for comparison because it highlights relations under reduced conditions that may be applied to a vertical traverse through a magma ocean (Hirschmann, 2012). Although such calculations are much more reduced than the experiments from this study, and

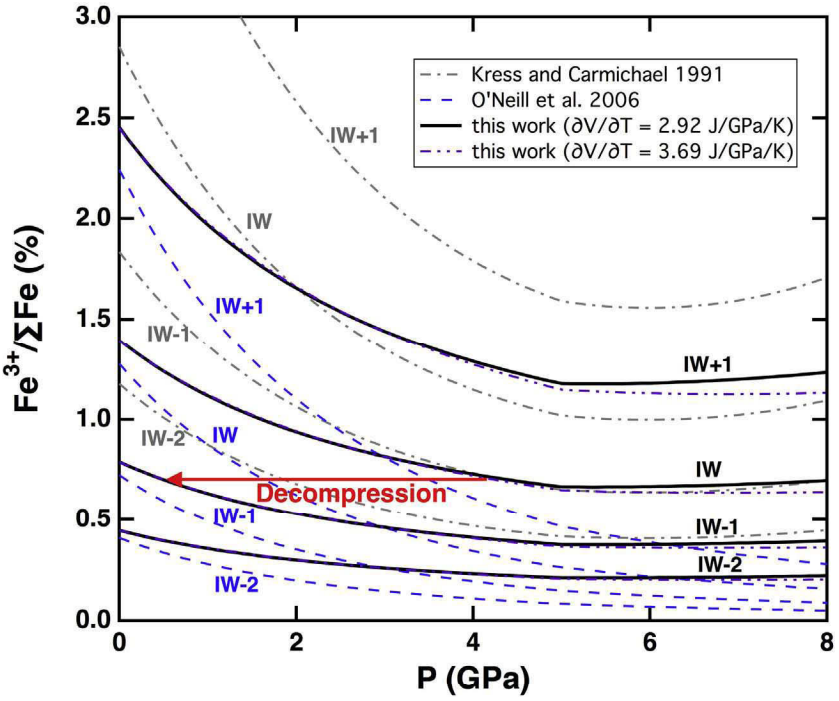

Fig. 10. $Fe^{3+}/\Sigma Fe$ of silicate melts as a function of pressure at oxygen fugacities fixed relative to the iron–wüstite (IW) buffer (calculated with Eq. (S2)) after Hirschmann (2012), for a (metastable) liquid with an FeO^* content similar to the bulk silicate earth (McDonough and Sun, 1995) at 1400 °C. Trends are calculated from the models obtained from this work, Kress and Carmichael (1991) (their Eq. (7)) and O'Neill et al. (2006). As illustrated by the red arrow, decompression at fixed values of $Fe^{3+}/\Sigma Fe$ leads to reduction relative to the IW buffer. Quantitative differences between the models are likely because all models are extrapolated from constraints obtained under more oxidizing conditions. The inflections at 5 GPa are owing to the calculation of the IW buffer, in which wüstite is assumed to be stoichiometric above 5 GPa, and of variable stoichiometry below 5 GPa (see Supplementary Materials).

therefore have much smaller $Fe^{3+}/\Sigma Fe$, extrapolation to such conditions is warranted, as previous work has shown that the volumetric properties of Fe^{2+} and Fe^{3+} in silicate melts mix approximately ideally (Kress and Carmichael, 1991; O'Neill et al., 2006). This extrapolation is also justified because the structural roles of the two cations do not vary strongly with $Fe^{3+}/\Sigma Fe$. For example, Mössbauer and XANES spectra of similar composition glasses quenched at 100 kPa indicate consistent CN for Fe^{3+} and Fe^{2+} across $Fe^{3+}/\Sigma Fe$ ratios from 0.07 to 0.80 (Zhang et al., 2016).

As shown in Fig. 10, melts at 1400 °C and held at the IW buffer have diminished $Fe^{3+}/\sum Fe$ with increasing pressure, analogous to the relations demonstrated experimentally at Ru-RuO_2 (Fig. 5). For melts not externally buffered, but rather held at constant $Fe^{3+}/\sum Fe$, isothermal decompression leads to reduction relative to the IW buffer (Fig. 10). This recapitulates the basic point made by Hirschmann (2012), that at low pressures an isochemical magma column, such as in a shallow magma ocean, becomes more oxidized relative to IW with increasing depth. A similar relationship is also suggested by the thermodynamic models of Kress and Carmichael (1991) and O'Neill et al. (2006) (Fig. 10). However, compared to these previous analyses, the revised model shows a smaller pressure dependence below 5 GPa. Also much of the dependence below 5 GPa derives from the anomalous behavior of the IW buffer at low pressure, as the stoichiometry of $Fe_{1-x}O$ changes (Fig. S5 and text in Supplementary Materials). Above 5 GPa, where $Fe_{1-x}O$ approaches stoichiometric FeO, variations in pressure along the IW buffer produce little change in $Fe^{3+}/\Sigma Fe$, indicating that compression or decompression of an isochemical melt corresponds to small changes in relative fO_2.

4.4. Applications to redox gradients in magma oceans

Magma oceans represent a pivotal stage in the chemical and dynamical evolution of terrestrial planets. Reactions between silicate magmas and transiting core-forming metal establish geochemical partitioning between the nascent mantle and core (Righter, 2003; Rubie et al., 2003, 2011; Wade and Wood, 2005; Rubie and Jacobson, 2015) and large-scale planetary degassing from magma oceans and associated silicate-vapor equilibration creates massive primitive atmospheres (Matsui and Abe, 1986; Zahnle et al., 2007; Elkins-Tanton, 2008; Hamada et al., 2013). The parameterization of $Fe^{3+}/\Sigma Fe$ as a function of T, P, and fO_2 can be applied to the problem of redox gradients in magma oceans (Hirschmann, 2012; Righter and Ghiorso, 2012a,b).

Redox relations in a magma ocean are dynamic, depending on the history of accreting material as well as the distribution of core-destined alloy and interactions with overlying atmospheres. One idealized end-member, discussed in detail in Hirschmann (2012) is a magma ocean in which metal has settled to the bottom, and is otherwise metal free. To a first approximation, one can consider that the convecting region above this depth is well-mixed, and therefore homogeneous in $Fe^{3+}/\Sigma Fe$ ratio (Hirschmann, 2012). The prevalence of equilibration of metal at depth is justified in part on inferences of the mean depth of metal–silicate equilibrium in the terrestrial magma ocean, which occurred at high pressure (e.g., >25 GPa for Earth, Li and Agee, 1996; Chabot et al., 2005; Corgne et al., 2008; Kegler et al., 2008). In such a magma ocean, the fO_2 at the base relative to IW is established by alloy-silicate equilibration at depth, and f_{O2} variations above that horizon are fixed by the $Fe^{3+}/\Sigma Fe$ of the magma itself, varying with pressure and temperature along the convecting magma ocean geotherm.

Such calculations can be applied to redox gradients in magma oceans applicable to the early differentiation of terrestrial planets and moons (Fig. 11). For magma oceans on small bodies such as Mercury and the Moon, the pressure at the base of a putative magma ocean is no more than that at the depth to the core mantle boundary of ~5 GPa (Garcia et al., 2011; Hauck et al., 2013), and the fO_2 at the magma ocean base is comparatively reduced. For these shallow magma oceans, the fO_2-pressure gradient is steep, owing chiefly to large changes in IW with pressure owing to changes in wüstite stoichiometry (Fig. S5) and so conditions are about 1.5 log unit more reduced at the surface than at the base (Fig. 11). Differences between the calculated trends for Mercury and the Moon are owing to different FeO contents of the silicate melts: 3 wt.% for Mercury, 9.37 wt.% for the Moon (Robinson and Taylor, 2001; Elardo et al., 2011).

On larger bodies, such as Mars or the Earth, the pressure at the base of the magma ocean can be higher and consequently the fO_2 relative to IW set at the base is significantly more reduced (Fig. 11). Our calculations for the Earth assume 25 GPa at the base of the magma ocean, though this is a minimum pressure for Earth (Li and Agee, 1996; Chabot et al., 2005; Corgne et al., 2008; Kegler et al., 2008), and for Mars assume 14 GPa (Rai and Westrenen, 2013; Yang et al., 2015). For the Earth and Mars, conditions at the surface of the magma ocean are approximately 2.5 and 2 orders of magnitude more reduced relative to IW than at the base, respectively, chiefly owing to the low pressure effects that derive from changes in wüstite stoichiometry.

We emphasize that the calculations above 7 GPa are extrapolations based on lower pressure experimental data. Our experimental and spectroscopic data indicate notable densification of Fe^{2+}-O components in the magma over this pressure range, but no appreciable change in coordination of Fe^{3+}-O polyhedra (Figs. 7 and 9). Our expectation, based on the increase in coordination of Fe^{3+} in minerals with pressure (e.g., Frost and McCammon, 2008), as well as the general trend of increase in coordination of cations in silicate melts with pressure (e.g., Ghiorso, 2004), is that Fe^{3+}-O coordination in silicate melts increases at some as-yet unknown pressure above 7 GPa, eventually leading to stabilization Fe^{3+} and increase in $Fe^{3+}/\Sigma Fe$ in silicate melts in equilibrium with metal alloy (Hirschmann, 2012). If this occurs, then near-surface conditions could be highly oxidizing for deep magma oceans on Earth or Mars.

The andesitic melts examined in this study are compositionally different from the peridotitic magmas expected in

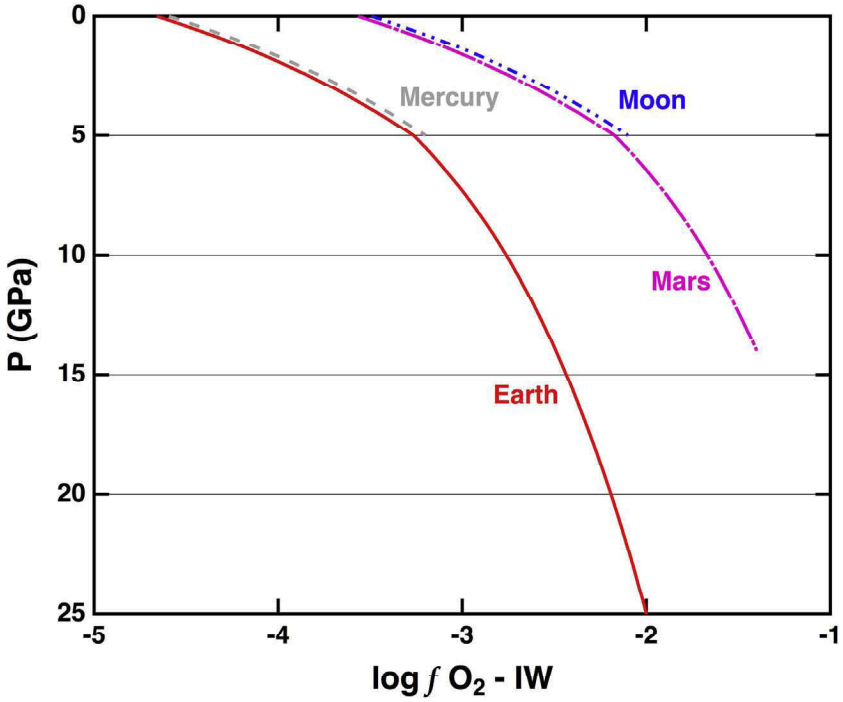

Fig. 11. Oxygen fugacity of silicate melts relative IW with FeO* from the bulk silicate composition for the Moon (9.37 wt%, Elardo et al., 2011), Mercury (3 wt%, Robinson and Taylor, 2001), Earth (8.05 wt%,McDonough and Sun, 1995), and Mars (18.71 wt%, Bertka and Fei, 1997) as a function of pressure at $Fe^{3+}/\Sigma Fe$ fixed at depth (5 GPa for Moon and Mercury, 25 GPa for Earth and 14 GPa for Mars) by equilibrium between iron and silicate melt (See Supplementary Materials). Note that the calculation assumes that metal is not present in the magma ocean except at its bottom, and therefore the $Fe^{3+}/\Sigma Fe$ ratio is constant, rather than being buffered by metal-silicate reaction, as is the case in Fig. 10. Trends are calculated from the models obtained from this work with the first column of parameters (Table 4) along the magma ocean adiabat of Stixrude et al. (2009). The adiabat temperatures (2200–3000 °C) are well above those in the experiments of this study (1400–1750 °C), and so the application to the redox state of magma oceans is an extrapolation. However, as the chief thermodynamic variables influencing the calculating trends here are the pressure derivatives of FeO and Fe_2O_3 partial molar volumes, and as the temperature derivatives of these pressure derivatives (e.g., $d^2V_i/dTdP$) are generally taken to be small or are neglected in silicate liquid equations of state (Ghiorso, 2004; Stixrude et al., 2009), this extrapolation is likely justifiable.

magma oceans and this could potentially affect depth-$Fe^{3+}/\Sigma Fe$-fO_2 relations. Although the $Fe^{3+}/\Sigma Fe$ ratio in silicate liquid fixed at a particular fO_2 depends on melt composition (e.g., Kress and Carmichael, 1991; Jayasuriya et al., 2004), the effect of pressure on the relationship between $Fe^{3+}/\Sigma Fe$ and fO_2 depends not on absolute $Fe^{3+}/\Sigma Fe$ but on its variations with pressure, which in turn derives from partial molar volume differences between FeO and Fe_2O_3 in the liquid. Several lines of evidence suggest that this relationship is not strongly dependent on melt composition. First, direct determinations of partial molar volumes of FeO and Fe_2O_3 do not show strong compositional dependences, except in the case of highly alkaline-rich melts (Lange and Carmichael, 1987; Kress and Carmichael, 1991). Second, partial molar volumes are strongly linked to coordination geometries (CN), and these are not greatly different for andesitic and more mafic melts. For example, coordination numbers of basalt and andesitic glasses quenched at 100 kPa are consistent within uncertainties (Fig. 8, Wilke et al., 2005; Zhang et al., 2016). Also, as discussed in Section 4.1, the pressure effect on CN of Fe^{2+} is qualitatively consistent between andesitic glass and fayalite liquid (Sanloup et al., 2013). Clearly, experiments analogous to those presented here but on ultramafic liquids are desirable, but the current results represent a reasonable first approximation of pressure-redox relations in a homogeneous magma column applied to magma oceans.

It should be clear that the calculations applied to magma oceans still have considerable uncertainties owing to lack of detailed information about the thermodynamics of FeO and Fe_2O_3 in silicate melts at high pressure. The relatively sophisticated equation of state for Fe-bearing silicate melts calibrated by Ghiorso (2004) and applied to magma oceans by Righter and Ghiorso (2012a,b) lacks treatment of Fe_2O_3. The absence of thermodynamic models for the behavior of Fe_2O_3 in high pressure silicate melts highlights the need for further experimental constraints on the effects of fO_2 and pressure on $Fe^{3+}/\Sigma Fe$.

5. CONCLUDING REMARKS

In general, shallow magma oceans equilibrated at depth with metal are more reduced at their surface than the fO_2 fixed by reaction between Fe-bearing silicate melt and coex-

isting metal. This means that atmospheres above shallow magma oceans will be highly reduced, and consist chiefly of H_2, CO, and NH_3 rather than H_2O, CO_2 and N_2 (Hirschmann, 2012). The experimental data presented here to 7 GPa demonstrates that this generalization holds for small planetary bodies such as Mercury and the Moon, and it also would apply to shallow magma oceans that could have existed at various times during the accretion of Earth and Mars. Whether it applies to deeper magma oceans relevant to larger planetary bodies requires constraints from experiments at higher pressures.

ACKNOWLEDGMENTS

We appreciate the assistance of Katherine Kelley, Fred Davis, Suzanne Birner, Tony Lanzirotti, and Matt Newville during XANES data collection, Peat Solheid for assistance in Mössbauer spectra collection, Anette von der Handt for aid with microprobe analyses, and Jed Mosenfelder for assistance and support in the experimental petrology laboratory. This paper also benefited from detailed critical comments from Raj Dasgupta, Jon Wade, and two anonymous referees. This work supported by the NASA Cosmochemistry program grant NNX11AG64G and ACW is supported by the NSERC Discovery program. Use of the APS and NSLS was supported by GUP ID 39997 and GUP 20395 respectively. Beamline X26A at the NSLS was supported by the Department of Energy (DOE) — Geosciences (DE-FG02-92ER14244 to The University of Chicago — CARS). Use of the NSLS was supported by DOE under Contract No. DE-AC02-98CH10886. GeoSoilEnviroCARS (Sector 13) at the APS is supported by the National Science Foundation — Earth Sciences (EAR-1128799) and Department of Energy — GeoSciences (DE-FG02-94ER14466). Use of the APS is supported by DOE under Contract No. DE-AC02-06CH11357.

APPENDIX A. SUPPLEMENTARY DATA

Supplementary data associated with this article can be found, in the online version, at http://dx.doi.org/10.1016/j.gca.2017.01.023.

REFERENCES

Alberto H. V., Pinto da Cunha J. L., Mysen B. O., Gil J. M. and Ayres de Campos N. (1996) Analysis of Mössbauer spectra of silicate glasses using a two-dimensional Gaussian distribution of hyperfine parameters. *J. Non-Cryst. Solids* **194**, 48–57.

Allwardt J. R., Stebbins J. F., Schmidt B. C., Frost D. J., Withers A. C. and Hirschmann M. M. (2005) Aluminum coordination and the densification of high-pressure aluminosilicate glasses. *Am. Mineral.* **90**, 1218–1222.

Armstrong L. S., Hirschmann M. M., Stanley B. D., Falksen E. G. and Jacobsen S. D. (2015) Speciation and solubility of reduced C-O-H-N volatiles in mafic melt: Implications for volcanism, atmospheric evolution, and deep volatile cycles in the terrestrial planets. *Geochim. Cosmochim. Acta* **171**, 283–302.

Berry A., O'Neill H., Jayasuriya K., Campbell S. and Foran G. (2003) XANES calibrations for the oxidation state of iron in a silicate glass. *Am. Mineral.* **88**, 967–977.

Berry A. J., O'Neill H. S. C., Scott D. R., Foran G. J. and Shelley J. M. G. (2006) The effect of composition on Cr^{2+}/Cr^{3+} in silicate melts. *Am. Mineral.* **91**, 1901–1908.

Bertka C. M. and Fei Y. (1997) Mineralogy of the Martian interior up to core-mantle boundary pressures. *J. Geophys. Res.: Solid Earth* **102**(1978–2012), 5251–5264.

Bézos A., Lorand J.-P., Humler E. and Gros M. (2005) Platinum-group element systematics in Mid-Oceanic Ridge basaltic glasses from the Pacific, Atlantic, and Indian Oceans. *Geochim. Cosmochim. Acta* **69**, 2613–2627.

Borisov A. and McCammon C. (2010) The effect of silica on ferric/ferrous ratio in silicate melts: An experimental study using Mössbauer spectroscopy. *Am. Mineral.* **95**, 545–555.

Botcharnikov R. E., Koepke J., Holtz F., McCammon C. and Wilke M. (2005) The effect of water activity on the oxidation and structural state of Fe in a ferro-basaltic melt. *Geochim. Cosmochim. Acta* **69**, 5071–5085.

Brearly M. (1990) Ferric iron in silicate melts in the system Na_2O-Fe_2O_3-SiO_2 at high pressure. *J. Geophys. Res.: Solid Earth* **95** (1978–2012), 15703–15716.

Campbell A. J., Danielson L., Righter K., Seagle C. T., Wang Y. and Prakapenka V. B. (2009) High pressure effects on the iron–iron oxide and nickel–nickel oxide oxygen fugacity buffers. *Earth Planet. Sci. Lett.* **286**, 556–564.

Chabot N. L., Draper D. S. and Agee C. B. (2005) Conditions of core formation in the earth: Constraints from Nickel and Cobalt partitioning. *Geochim. Cosmochim. Acta* **69**, 2141–2151.

Chi H., Dasgupta R., Duncan M. S. and Shimizu N. (2014) Partitioning of carbon between Fe-rich alloy melt and silicate melt in a magma ocean–Implications for the abundance and origin of volatiles in Earth, Mars, and the Moon. *Geochim. Cosmochim. Acta* **139**, 447–471.

Christie D. M., Carmichael I. S. E. and Langmuir C. H. (1986) Oxidation states of mid-ocean ridge basalt glasses. *Earth Planet. Sci. Lett.* **79**, 397–411.

Cooper R. F., Fanselow J. B. and Poker D. B. (1996) The mechanism of oxidation of a basaltic glass: chemical diffusion of network-modifying cations. *Geochim. Cosmochim. Acta* **60**, 3253–3265.

Corgne A., Keshav S., Wood B., McDonough W. and Fei Y. (2008) Metal–silicate partitioning and constraints on core composition and oxygen fugacity during Earth accretion. *Geochim. Cosmochim. Acta* **72**, 574–589.

Cottrell E. and Kelley K. A. (2011) The oxidation state of Fe in MORB glasses and the oxygen fugacity of the upper mantle. *Earth Planet. Sci. Lett.* **305**, 270–282.

Cottrell E., Kelley K. A., Lanzirotti A. and Fischer R. A. (2009) High-precision determination of iron oxidation state in silicate glasses using XANES. *Chem. Geol.* **268**, 167–179.

Dasgupta R., Hirschmann M. M. and Withers A. C. (2004) Deep global cycling of carbon constrained by the solidus of anhydrous, carbonated eclogite under upper mantle conditions. *Earth Planet. Sci. Lett.* **227**, 73–85.

Dasgupta R., Chi H., Shimizu N., Buono A. S. and Walker D. (2013) Carbon solution and partitioning between metallic and silicate melts in a shallow magma ocean: Implications for the origin and distribution of terrestrial carbon. *Geochim. Cosmochim. Acta* **102**, 191–212.

Dauphas N., Roskosz M., Alp E., Neuville D., Hu M., Sio C., Tissot F., Zhao J., Tissandier L., Medard E. and Cordier C. (2014) Magma redox and structural controls on iron isotope variations in Earth's mantle and crust. *Earth Planet. Sci. Lett.* **398**, 127–140.

Dingwell D. B., Brearley M. and Dickinson, Jr., J. E. (1988) Melt densities in the Na_2O-FeO-Fe_2O_3-SiO_2 system and the partial molar volume of tetrahedrally-coordinated ferric iron in silicate melts. *Geochim. Cosmochim. Acta* **52**, 2467–2475.

Dyar M. D. (1985) A review of Mössbauer data on inorganic glasses: the effects of composition on iron valency and coordination. *Am. Mineral.* **70**, 304–316.

Dyar M. D., Naney M. T. and Swanson S. E. (1987) Effects of quench methods on Fe^{3+}/Fe^{2+} ratios: A Mössbauer and wet-chemical study. *Am. Mineral.* **72**, 792–800.

Dyar M., Agresti D., Schaefer M., Grant C. and Stlute E. (2006) Mössbauer spectroscopy of Earth and planetary materials. *Annu. Rev. Earth Planet. Sci.* **34**, 83–125.

Elardo S. M., Draper D. S. and Shearer C. K. (2011) Lunar Magma Ocean crystallization revisited: Bulk composition, early cumulate mineralogy, and the source regions of the highlands Mg-suite. *Geochim. Cosmochim. Acta* **75**, 3024–3045.

Elkins-Tanton L. (2008) Linked magma ocean solidification and atmospheric growth for Earth and Mars. *Earth Planet. Sci. Lett.* **271**, 181–191.

Frost D. J. and McCammon C. A. (2008) The redox state of Earth's mantle. *Annu. Rev. Earth Planet. Sci.* **36**, 389–420.

Frost D. J., Liebske C., Langenhorst F., McCammon C. A., Trønnes R. G. and Rubie D. C. (2004) Experimental evidence for the existence of iron-rich metal in the Earth's lower mantle. *Nature* **428**, 409–412.

Gaillard F., Scaillet B. and Pichavant M. (2002) Kinetics of iron oxidation-reduction in hydrous silicic melts. *Am. Mineral.* **87**, 829–837.

Gaillard F., Pichavant M. and Scaillet B. (2003a) Experimental determination of activities of FeO and Fe_2O_3 components in hydrous silicic melts under oxidizing conditions. *Geochim. Cosmochim. Acta* **67**, 4389–4409.

Gaillard F., Schmidt B., Mackwell S. and McCammon C. (2003b) Rate of hydrogen–iron redox exchange in silicate melts and glasses. *Geochim. Cosmochim. Acta* **67**, 2427–2441.

Garcia R. F., Gagnepain-Beyneix J., Chevrot S. and Lognonné P. (2011) Very preliminary reference Moon model. *Phys. Earth Planet. Inter.* **188**, 96–113.

Ghiorso M. S. (2004) An equation of state for silicate melts. I. Formulation of a general model. *Am. J. Sci.* **304**, 637–678.

Giuli G., Paris E., Hess K., Dingwell D., Cicconi M., Eeckhout S., Fehr K. and Valenti P. (2011) XAS determination of the Fe local environment and oxidation state in phonolite glasses. *Am. Mineral.* **96**, 631–636.

Guo X., Lange R. A. and Ai Y. (2014) Density and sound speed measurements on model basalt (An–Di–Hd) liquids at one bar: New constraints on the partial molar volume and compressibility of the FeO component. *Earth Planet. Sci. Lett.* **388**, 283–292.

Hamada M., Ushioda M., Fujii T. and Takahashi E. (2013) Hydrogen concentration in plagioclase as a hygrometer of arc basaltic melts: Approaches from melt inclusion analyses and hydrous melting experiments. *Earth Planet. Sci. Lett.* **365**, 253–262.

Hauck S. A., Margot J. L., Solomon S. C., Phillips R., Johnson C. L., Lemoine F. G., Mazarico E., McCoy T. J., Padovan S., Peale S. J., Perry M. E., Smith D. E. and Zuber M. J. (2013) The curious case of Mercury's internal structure. *J. Geophys. Res.* **118**, 1204–1220.

Helgason Ö., Steinthorsson S. and Mørup S. (1989) The ferric/ferrous ratio in basalt melts at different oxygen pressures. *Hyperfine Interactions* **45**.

Hirschmann M. M. (2012) Magma ocean influence on early atmosphere mass and composition. *Earth Planet. Sci. Lett.* **341**, 48–57.

Holland T. I. M. and Powell R. (2001) Calculation of phase relations involving haplogranitic melts using an internally consistent thermodynamic dataset. *J. Petrol.* **42**, 673–683.

Jayasuriya K. D., O'Neill H. S. C., Berry A. J. and Campbell S. J. (2004) A Mössbauer study of the oxidation state of Fe in silicate melts. *Am. Mineral.* **89**, 1597–1609.

Jochum K., Willbold M., Raczek I., Stoll B. and Herwig K. (2005) Chemical characterisation of the USGS reference glasses GSA-1G, GSC-1G, GSD-1G, GSE-1G, BCR-2G, BHVO-2G and BIR-1G using EPMA, ID-TIMS, ID-ICP-MS and LA-ICP-MS. *Geostand. Geoanal. Res.*, 29.

Jochum K., Stoll B., Herwig K., Willbold M., Hofmann A., Amini M., Aarburg S., Abouchami W., Hellebrand E., Mocek B., Raczek I., Stracke A., Alard O., Bouman C., Becker S., Dücking M., Brätz H., Klemd R., Bruin D., Canil D., Cornell D., Hoog C.-J., Dalpé C., Danyushevsky L., Eisenhauer A., Gao Y., Snow J., Groschopf N., Günther D., Latkoczy C., Guillong M., Hauri E., Höfer H., Lahaye Y., Horz K., Jacob D., Kasemann S., Kent A., Ludwig T., Zack T., Mason P., Meixner A., Rosner M., Misawa K., Nash B., Pfänder J., Premo W., Sun W., Tiepolo M., Vannucci R., Vennemann T., Wayne D. and Woodhead J. (2006) MPI-DING reference glasses for in situ microanalysis: New reference values for element concentrations and isotope ratios. *Geophys. Geosyst.*, 7.

Kegler P., Holzheid A., Frost D., Rubie D., Dohmen R. and Palme H. (2008) New Ni and Co metal-silicate partitioning data and their relevance for an early terrestrial magma ocean. *Earth Planet. Sci. Lett.* **268**, 28–40.

Kilinc A., Carmichael I., Rivers M. and Sack R. (1983) The ferric-ferrous ratio of natural silicate liquids equilibrated in air. *Contrib. Miner. Petrol.* **83**, 136–140.

Kress V. C. and Carmichael I. S. E. (1988) Stoichiometry of the iron oxidation reaction in silicate melts. *Am. Mineral.* **73**, 1267–1274.

Kress V. and Carmichael I. (1991) The compressibility of silicate liquids containing Fe_2O_3 and the effect of composition, temperature, oxygen fugacity and pressure on their redox states. *Contrib. Miner. Petrol.* **108**, 82–92.

Lagarec K. and Rancourt D. G. (1997) Extended Voigt-based analytic lineshape method for determining N-dimensional correlated hyperfine parameter distributions in Mössbauer spectroscopy. *Nucl. Instrum. Methods Phys. Res., Sect. B* **129**, 266–280.

Lange R. A. and Carmichael I. S. E. (1987) Densities of Na_2O-K_2O-CaO-MgO-FeO-Fe_2O_3-Al_2O_3-TiO_2-SiO_2 liquids: New measurements and derived partial molar properties. *Geochim. Cosmochim. Acta* **51**, 2931–2946.

Lange R. A. and Carmichael I. S. E. (1989) Ferric-ferrous equilibria in Na_2O-FeO-Fe_2O_3-SiO_2 melts - effects of analytical techniques on derived partial molar volumes. *Geochim. Cosmochim. Acta* **53**, 2195–2204.

Li J. and Agee C. B. (1996) Geochemistry of mantle–core differentiation at high pressure. *Nature* **381**, 686–689.

Liu Q. and Lange R. A. (2006) The partial molar volume of Fe_2O_3 in alkali silicate melts: Evidence for an average Fe^{3+} coordination number near five. *Am. Mineral.* **91**, 385–393.

Magnien V., Neuville D. R., Cormier L., Mysen B. O., Briois V., Belin S., Pinet O. and Richet P. (2004) Kinetics of iron oxidation in silicate melts: a preliminary XANES study. *Chem. Geol.* **213**, 253–263.

Matsui T. and Abe Y. (1986) Evolution of an impact-induced atmosphere and magma ocean on the accreting Earth. *Nature* **319**, 303–305.

McCammon C. (1997) Ferric iron content of mineral inclusions in diamonds from Säo Luiz: a view into the lower mantle. *Science* **278**, 434–436.

McDonough W. F. and Sun S. S. (1995) The composition of the Earth. *Chem. Geol.* **120**, 223–253.

Miller G. H., Stolper E. M. and Ahrens T. J. (1991) The equation of state of a molten komatiite: 1 shock wave compression to 36 GPa. *J. Geophys. Res.: Solid Earth* **96**(1978–2012), 11831–11848.

Mo X., Carmichael I. S. E., Rivers M. and Stebbins J. (1982) The partial molar volume of Fe_2O_3 in multicomponent silicate liquids and the pressure dependence of oxygen fugacity in magmas. *Mineral. Mag.* **45**, 237–245.

Mysen B. O. and Virgo D. (1985) Iron-bearing silicate melts: relations between pressure and redox equilibria. *Phys. Chem. Miner.* **12**, 191–200.

Neuville D. R., Courtial P., Dingwell D. B. and Richet P. (1993) Thermodynamic and rheological properties of rhyolite and andesite melts. *Contrib. Miner. Petrol.* **113**, 572–581.

O'Neill H. S. C., McCammon C. A., Canil D., Rubie D. C. and Ross C. R. (1993) Mössbauer spectroscopy of mantle transition zone phases and determination of minimum Fe^{3+} content. *Am. Mineral.* **78**, 456–460.

Ohtani E., Hirao N., Kondo T., Ito M. and Kikegawa T. (2005) Iron-water reaction at high pressure and temperature, and hydrogen transport into the core. *Phys. Chem. Miner.* **32**, 77–82.

O'Neill H. S. C. (1991) The origin of the Moon and the early history of the Earth—A chemical model. Part 2: The Earth. *Geochim. Cosmochim. Acta* **55**, 1159–1172.

O'Neill H. S. C. and Nell J. (1997) Gibbs free energies of formation of RuO_2, IrO_2, and OsO_2: A high-temperature electrochemical and calorimetric study. *Geochim. Cosmochim. Acta* **61**, 5279–5293.

O'Neill H. S. C., Berry A. J., McCammon C., Jayasuriya K. D., Campbell S. J. and Foran G. (2006) An experimental determination of the effect of pressure on the $Fe^{3+}/\Sigma Fe$ ratio of an anhydrous silicate melt to 3.0 GPa. *Am. Mineral.* **91**, 404–412.

Partzsch G. M., Lattard D. and McCammon C. (2004) Mössbauer spectroscopic determination of Fe^{3+}/Fe^{2+} in synthetic basaltic glass: a test of empirical fO_2 equations under superliquidus and subliquidus conditions. *Contrib. Miner. Petrol.* **147**, 565–580.

Pawley A. R., Holloway J. R. and McMillan P. F. (1992) The effect of oxygen fugacity on the solubility of carbon-oxygen fluids in basaltic melt. *Earth Planet. Sci. Lett.* **110**, 213–225.

Rai N. and Westrenen W. (2013) Core-mantle differentiation in Mars. *J. Geophys. Res.: Planets* **118**, 1195–1203.

Rigden S. M., Ahrens T. J. and Stolper E. M. (1989) High-pressure equation of state of molten anorthite and diopside. *J. Geophys. Res.: Solid Earth* **94**(1978–2012), 9508–9522.

Righter K. (2003) Metal-silicate partitioning of siderophile elements and core formation in the Early Earth. *Annu. Rev. Earth Planet. Sci.* **31**, 135–174.

Righter K. and Ghiorso M. (2012a) Redox systematics of a magma ocean with variable pressure-temperature gradients and composition. *Proc. Natl. Acad. Sci.* **109**, 11955–11960.

Righter K. and Ghiorso M. (2012b) Correction for Righter and Ghiorso, Redox systematics of a magma ocean with variable pressure-temperature gradients and composition. *Proc. Natl. Acad. Sci.* **109**, 16749–16750.

Rivers M. L. and Carmichael I. S. E. (1987) Ultrasonic studies of silicate melts. *J. Geophys. Res.: Solid Earth* **92**(1978–2012), 9247–9270.

Robinson M. and Taylor G. (2001) Ferrous oxide in Mercury's crust and mantle. *Meteorit. Planet. Sci.* **36**, 841–847.

Rohrbach A., Ballhaus C., Schindler U., Ulmer P., Kamenetsky V. and Kuzmin D. (2007) Metal saturation in the upper mantle. *Nature* **449**, 456–458.

Roskosz M., Bouhifd M. A., Jephcoat A., Marty B. and Mysen B. (2013) Nitrogen solubility in molten metal and silicate at high pressure and temperature. *Geochim. Cosmochim. Acta* **121**, 15–28.

Rossano S., Balan E., Morin G., Bauer J. P., Calas G. and Brouder C. (1999) Fe Mössbauer spectroscopy of tektites. *Phys. Chem. Miner.* **26**, 530–538.

Rossano S., Behrens H. and Wilke M. (2008) Advanced analyses of ^{57}Fe Mössbauer data of alumino-silicate glasses. *Phys. Chem. Miner.* **35**, 77–93.

Rubie D. C. and Jacobson S. A. (2015) *Mechanisms and Geochemical Models of Core Formation. Deep Earth: Physics and Chemistry of the Lower Mantle and Core*, pp. 181–190.

Rubie D., Melosh H., Reid J., Liebske C. and Righter K. (2003) Mechanisms of metal–silicate equilibration in the terrestrial magma ocean. *Earth Planet. Sci. Lett.* **205**, 239–255.

Rubie D., Frost D., Mann U., Asahara Y., Nimmo F., Tsuno K., Kegler P., Holzheid A. and Palme H. (2011) Heterogeneous accretion, composition and core-mantle differentiation of the Earth. *Earth Planet. Sci. Lett.* **301**, 31–42.

Rubie D. C., Jacobson S. A., Morbidelli A., O'Brien D. P., Young E. D., de Vries J., Nimmo F., Palme H. and Frost D. (2015) Accretion and differentiation of the terrestrial planets with implications for the compositions of early-formed Solar System bodies and accretion of water. *Icarus* **248**, 89–108.

Ryan M. P. and Sammis C. G. (1981) The glass transition in basalt. *J. Geophys. Res.* **86**, 9519–9535.

Sack R., Carmichael I., Rivers M. and Ghiorso M. (1980) Ferric-ferrous equilibria in natural silicate liquids at 1 bar. *Contrib. Miner. Petrol.* **75**, 369–376.

Sanloup C., Drewitt J. W. E., Crépisson C., Kono Y., Park C., McCammon C., Hennet L., Brassamin S. and Bytchkov A. (2013) Structure and density of molten fayalite at high pressure. *Geochim. Cosmochim. Acta* **118**, 118–128.

Stanley B., Hirschmann M. and Withers A. (2014) Solubility of COH volatiles in graphite-saturated martian basalts. *Geochim. Cosmochim. Acta* **129**, 54–76.

Stevenson D. J. (1977) Hydrogen in the Earth's core. *Nature* **268**, 130–131.

Stixrude L., de Koker N., Sun N., Mookherjee M. and Karki B. B. (2009) Thermodynamics of silicate liquids in the deep Earth. *Earth Planet. Sci. Lett.* **278**, 226–232.

Tenner T. J., Hirschmann M. M., Withers A. C. and Ardia P. (2012) H_2O storage capacity of olivine and low-Ca pyroxene from 10 to 13 GPa: consequences for dehydration melting above the transition zone. *Contrib. Miner. Petrol.* **163**, 297–316.

Thornber C. R., Roeder P. L. and Foster J. R. (1980) The effect of composition on the ferric-ferrous ratio in basaltic liquids at atmospheric pressure. *Geochim. Cosmochim. Acta* **44**, 525–532.

Wade J. and Wood B. (2005) Core formation and the oxidation state of the Earth. *Earth Planet. Sci. Lett.* **236**, 78–95.

Wetzel D. T., Rutherford M. J., Jacobsen S. D., Hauri E. H. and Saal A. E. (2013) Degassing of reduced carbon from planetary basalts. *Proc. Natl. Acad. Sci.* **110**, 8010–8013.

Wilke M., Farges F., Petit P.-E., Brown, Jr, Gordon E. and Martin F. (2001) Oxidation state and coordination of Fe in minerals: An Fe K-XANES spectroscopic study. *Am. Mineral.* **86**, 714–730.

Wilke M., Behrens H., Burkhard D. and Rossano S. (2002) The oxidation state of iron in silicic melt at 500 MPa water pressure. *Chem. Geol.* **189**, 55–67.

Wilke M., Partzsch G. M., Bernhardt R. and Lattard D. (2005) Determination of the iron oxidation state in basaltic glasses using XANES at the K-edge. *Chem. Geol.* **220**, 143–161.

Wilke M., Schmidt C., Farges F., Malavergne V., Gautron L., Simionovici A., Hahn M. and Petit P.-E. (2006) Structural environment of iron in hydrous aluminosilicate glass and melt-

evidence from X-ray absorption spectroscopy. *Chem. Geol.* **229**, 144–161.

Wilke M., Farges F. and Partzsch G. (2007) Speciation of Fe in silicate glasses and melts by in-situ XANES spectroscopy. *Am. Mineral.* **92**, 44–56.

Williams Q. and Jeanloz R. (1988) Spectroscopic evidence for pressure-induced coordination changes in silicate glasses and melts. *Science* **239**, 902–905.

Xirouchakis D., Hirschmann M. M. and Simpson J. A. (2001) The effect of titanium on the silica content and on mineral-liquid partitioning of mantle-equilibrated melts. *Geochim. Cosmochim. Acta* **65**, 2201–2217.

Yang S., Humayun M., Righter K., Jefferson G., Fields D. and Irving A. J. (2015) Siderophile and chalcophile element abundances in shergottites: Implications for Martian core formation. *Meteorit. Planet. Sci.* **50**, 691–714.

Zahnle K., Arndt N., Cockell C., Halliday A., Nisbet E., Selsis F. and Sleep N. (2007) Emergence of a habitable planet. *Space Sci. Rev.* **129**, 35–78.

Zhang Z. and Hirschmann M. M. (2016) Experimental constraints on mantle sulfide melting up to 8 GPa. *Am. Mineral.* **101**, 181–192.

Zhang H. L., Solheid P. A., Lange R. A., Von Der Handt A. and Hirschmann M. M. (2015) Accurate determination of Fe3+/ΣFe of andesitic glass by Mössbauer spectroscopy. *Am. Mineral.* **100**, 1967–1977.

Zhang H. L., Hirschmann M. M., Cottrell E., Newville M. and Lanzirotti A. (2016) Structural environment of iron and accurate determination of Fe3+/ΣFe ratios in andesitic glasses by XANES and Mössbauer spectroscopy. *Chem. Geol.* **428**, 48–58.

Associate editor: Rajdeep Dasgupta